

Ingredients of the planet-formation puzzle: Gas substructures and kinematics in transition discs Wölfer. L.B.

#### Citation

Wölfer, L. B. (2023, March 28). *Ingredients of the planet-formation puzzle: Gas substructures and kinematics in transition discs*. Retrieved from https://hdl.handle.net/1887/3589823

Version: Publisher's Version

Licence agreement concerning inclusion of doctoral

License: thesis in the Institutional Repository of the University

of Leiden

Downloaded from: <a href="https://hdl.handle.net/1887/3589823">https://hdl.handle.net/1887/3589823</a>

**Note:** To cite this publication please use the final published version (if applicable).

McCoy: So what's your problem?

Spock: Acceleration is no longer a constant. McCoy: Well, then you're just gonna have

to take your best shot. Spock: Best shot?

McCoy: Guess, Spock. Your best guess. Spock: Guessing is not in my nature, Doctor.

McCoy: Well, nobody's perfect.

Star Trek IV: The Voyage Home

Chapter 4

## Kinematics and brightness temperatures of transition discs

A survey of gas substructures as seen with ALMA

L. Wölfer, S. Facchini, N. van der Marel, E. F. van Dishoeck, M. Benisty, A. J. Bohn, L. Francis, A. F. Izquierdo, R. Teague

#### ABSTRACT

Context. In recent years, high-angular-resolution observations of the dust and gas content in circumstellar discs have revealed a variety of morphologies, naturally triggering the question of whether these substructures are driven by forming planets interacting with their environment or other mechanisms. While it remains difficult to directly image embedded planets, one of the most promising methods to distinguish disc-shaping mechanisms is to study the kinematics of the gas disc. Characterizing deviations from Keplerian rotation can then be used to probe underlying perturbations such as planet—disc interactions. Creating spiral structures, the latter can also be traced in the brightness temperature.

**Aims.** In this paper we aim to analyse the gas brightness temperatures and kinematics of a sample of 36 transition discs observed with the Atacama Large Millimeter/submillimeter Array (ALMA) to resolve and characterize possible substructures that may be tracing embedded companions.

**Methods.** For our analysis, we use archival Band 6 and Band 7 ALMA observations of different CO isotopologues (<sup>12</sup>CO, <sup>13</sup>CO, and C<sup>18</sup>O) and fit different Keplerian disc models (thin and thick disc geometry) to the retrieved velocity field of each disc.

Results. After the subtraction of an azimuthally averaged brightness temperature profile and Keplerian rotation model from the peak brightness temperature and velocity maps, we find significant substructures in eight sources of our sample (CQ Tau, GG Tau, HD 100453, HD 142527, HD 169142, HP Cha, TW Hya, and UX Tau A) in both the brightness temperature and velocity residuals. Other sources show tentative features, while about half of our sample does not show any substructures in the temperature and kinematics that may be indicative of planet—disc interactions.

Conclusions. For the first time, we compare the substructures from our analysis with various other indicators for the presence of planets. About 20% of discs show strong features such as arcs or spirals, possibly associated with the presence of planets, while the majority of discs do not present as clear planet-driven signatures. Almost all discs that exhibit spirals in near-infrared scattered light show at least tentative features in the CO data. The present data are able to reveal only very massive bodies and a lack of features may suggest that, if there are planets at all, they are of lower mass ( $< 1\text{-}3\,M_{\rm J}$ ) or may be located closer to the star within deep cavities. Deeper and higher resolution observations and modelling efforts are needed to confirm such scenarios.

#### 4.1 Introduction

Circumstellar discs are formed as a consequence of angular momentum conservation during the process of star formation when material from a molecular cloud core is channeled towards the newborn star in the centre. Also called protoplanetary or planet-forming discs, they provide the gas and dust needed for the formation of planetary systems such as our Solar System. Far from being static, they evolve and eventually disperse while birthing planets, with different mechanisms shaping their appearance and the planet formation processes. At the same time, planets interact with their environment and are expected to alter their host disc's structure, leaving observable marks depending on their mass and location in the disc.

In the last decade, high-angular-resolution dust and gas observations with the Atacama Large Millimeter/submillimeter Array (ALMA; ALMA Partnership et al. 2015) as well as near-infrared (NIR) scattered light observations with, for example, the Spectro-Polarimetric High-contrast Exoplanet REsearch (SPHERE; Beuzit et al. 2019), the Gemini Planet Imager (GPI; Macintosh et al. 2014), or the Subaru telescope's High-Contrast Coronographic Imager for Adaptive Optics (Hi-CIAO), equipped with the Extreme Adaptive Optics System (SCExAO; Jovanovic et al. 2015) have indeed shown that a variety of substructures, such as gaps or even cavities, rings, spiral arms, and azimuthal asymmetries, are ubiquitous in both the dust and the gas component of planet-forming discs (e.g., van der Marel et al. 2013; Benisty et al. 2015, 2017, 2018; Casassus 2016; Andrews et al. 2018; Cazzoletti et al. 2018; Long et al. 2018; Andrews 2020; Uyama et al. 2020).

Even though there exist several mechanisms that may explain these observations, such as gravitational instabilities (e.g., Kratter & Lodato 2016), photoevaporation (e.g., Owen et al. 2011; Picogna et al. 2019), magnetorotational instabilities (e.g., Flock et al. 2015, 2017; Riols & Lesur 2019), zonal flows (e.g., Uribe et al. 2015), or compositional baroclinic instabilities (e.g., Klahr & Bodenheimer 2004), at least some of the substructures are expected to be linked to the presence of (massive) planets (Lin & Papaloizou 1979; Zhang et al. 2018). To interpret the origin of the various substructures, it is crucial to understand how common they are, if they follow certain patterns, and if differences or similarities can be identified for different star-disc system morphologies.

One particularly interesting subgroup of young stellar objects (YSOs) is represented by the so-called transition discs. Originally identified through a lack of infrared (IR) excess in their spectral energy distribution (SED; Strom et al. 1989), they are characterized by dust (and gas) depleted inner regions (e.g., Espaillat et al. 2014; Ercolano & Pascucci 2017). While they are sometimes classified as an intermediate state between a full optically thick disc and disc dispersal, planet—disc interactions provide an alternative explanation for the observed cavities. At least some transition discs — especially those with very deep dust and gas cavities (e.g., van der Marel et al. 2016) — are expected to be the result of the dynamical clearing of a massive companion that is either planetary or binary. This may imply that transition discs are not an evolutionary state that every disc goes through, since massive planets (or binary companions) are not found around every star (e.g., Johnson et al. 2010; Nielsen et al. 2019; van der Marel & Mulders 2021). Tran-

sition discs, therefore, represent excellent candidates to catch planet formation in action, test planet formation models, and probe disc evolution mechanisms.

To unambiguously link the observed substructures to the presence of a planet, the latter needs to be directly imaged in its environment. However, this method is only feasible for very bright and massive planets that are not severely affected by dust extinction (Sanchis et al. 2020). To date, the only system in which a robust direct detection of proto-planets has been obtained is PDS 70, hosting two planets with masses of several  $M_{\rm J}$  (Keppler et al. 2018; Haffert et al. 2019; Benisty et al. 2021).

Alternatively we can study the indirect effects that planets may have on the dust and gas distributions. In this context, one promising method is to investigate the kinematics to look for perturbations that are induced in the velocity field of the rotating gas. Identifying deviations from Keplerian rotation can then be used to probe the local pressure gradient and to characterize the shape of the perturbation. Teague et al. (2018a) used this technique to constrain the rotation profile of HD 163296 and its deviation from a Keplerian profile. In addition, Teague et al. (2019a) report significant meridional flows in that disc. Evidence of similar meridional flows was found in HD 169142 by Yu et al. (2021). The kinematics of AS 209 were studied by Teague et al. (2018b) and Rosotti et al. (2020b) who measured the gas-dust coupling as well as the width of gas pressure bumps and report a vertical dependence on the pressure maxima. So-called kink features were detected by Pinte et al. (2018b, 2019) in the iso-velocity curves of HD 163296 and HD 97048 that are consistent with a Jupiter-mass planet. A possible signature of an embedded planet was also found by Casassus & Pérez (2019) in the HD 100546 disc in the form of a Doppler flip in the residual kinematics. In TW Hya (Teague et al. 2019b), HD 100453 (Rosotti et al. 2020a), HD 135344B (Casassus et al. 2021), CQ Tau (Wölfer et al. 2021), and HD 163296 and MWC 480 (Teague et al. 2021), spiral structures are seen in the kinematics after subtraction of a Keplerian model, which is possibly connected to a companion. Non-Keplerian gas spirals are further detected in HD 142527 by Garg et al. (2021). Calcino et al. (2022) show that the outer kink in HD 163296 is possibly associated with a planetary spiral wake. Izquierdo et al. (2021) developed a new, channel-map-fitting package to robustly identify localized velocity perturbations in both radius and azimuth and thus infer the position of an embedded planet. Applied to HD 163296 data, they are able to find indications for two embedded planets with this method (Izquierdo et al. 2022).

In addition to the kinematics, it can also be useful to look for substructures or asymmetries in the peak intensity (brightness temperature) residuals in the search for evidence of companions. The density waves created by a companion result in an increase in surface density and thus in a higher opacity. This moves the  $\tau=1$  layer to a higher altitude where the temperature is generally higher, resulting in spiral substructures in the gas brightness temperature (Phuong et al. 2020a,b). In addition, planets can generate tightly wound spirals in the brightness temperature through buoyancy resonances (Bae et al. 2021). The temperature structure in planet-driven spiral arms was investigated by Muley et al. (2021) and their models may explain the observed thermal features in discs such as TW Hya

and CQ Tau: Teague et al. (2019b) and Wölfer et al. (2021) report the detection of spiral structures in the <sup>12</sup>CO brightness temperature of TW Hya and CQ Tau, respectively, after the subtraction of an azimuthally averaged model. These spirals are (at least partly) linked to the spirals observed in the velocity residuals (for TW Hya, see also Sturm et al. 2020), and in the case of CQ Tau they are connected to a small spiral in the NIR (Uyama et al. 2020).

Studying the gas component in discs may enable one to assess the different dynamical processes described above that are shaping the disc and reveal previously undetected substructures. In this context, probing different disc layers with various molecules may help distinguish between the formation mechanisms of the observed substructures (e.g., Pinte et al. 2018a; Law et al. 2021a). For example, in a passively heated disc with a positive vertical temperature gradient, more tightly wound spirals are expected towards the midplane in the planetary scenario, while similar spiral pitch angles would be established between the surface and midplane layers if resulting from gravitational instabilities (Juhász & Rosotti 2018). Furthermore, an embedded planet induces perturbations in all three velocity components, which vary as a function of height: The magnitude of radial and rotational perturbations ( $v_r$ ,  $v_\varphi$ ) decreases and that of vertical perturbations ( $v_z$ ) increases towards the disc surface (Pinte et al. 2019).

To this point, the connection between inner and outer disc structures in protoplanetary discs is not fully understood, but it represents an important piece in the planet-formation puzzle. Several observations of transition discs in NIR scattered light have revealed dark regions (e.g., Stolker et al. 2016; Casassus et al. 2018), which are commonly interpreted as shadows resulting from a misalignment between the inner and the outer disc (e.g., Marino et al. 2015; Facchini et al. 2018). One particularly exciting explanation for this is the presence of (a) massive misaligned companion(s) inducing a misalignment in specific disc regions around them (Francis & van der Marel 2020; Perraut & Gravity Collaboration 2021; Bohn et al. 2022).

In this work, we investigate archival CO data of a sample of 36 transition discs in terms of both their velocity and brightness temperature structure to search for possible perturbations and features that may be linked to the presence of embedded companions. The paper is structured as follows: In Sect. 4.2, we give an overview of the selected targets. The observational results, including brightness temperature and velocity maps as well as radial intensity profiles, are presented in Sect. 4.3. In Sect. 4.4, we describe our analysis, showing the resulting velocity and brightness temperature residuals. These results are discussed in Sect. 4.5 where a comparison with other indicators of planets is done. A summary of our work is presented in Sect. 4.6.

## 4.2 Observations

Our selected sample consists of 36 transition discs, chosen from the sample of Francis & van der Marel (2020) where sufficient CO data are available. Except for TW Hya, these discs show large (> 25 au) inner dust cavities and therefore

represent the ideal candidates to search for planet–disc interactions. It comprises different star-disc system architectures, including a range of spectral types (M2 to A0; primary) and stellar masses (0.4  $M_{\odot}$  to 2.6  $M_{\odot}$ , primary), counting 23 TTauri and 13 Herbig stars. Some stellar and disc properties of our targets are listed in Table 4.1.

For our analysis, we collected either Band 6 or Band 7 archival CO line data, observed with ALMA. For most sources (two-thirds), we used re-imaged (and self-calibrated) data cubes that are either public or were obtained via private communication; for the remaining sources, we used archival data products. This is indicated in Table 4.2, where some characteristics of the data cubes are listed for the main lines used in our study. Typical spectral resolutions of the data are a few  $100~{\rm m\,s^{-1}}$  and spatial resolutions lie between  $\sim 6{-}135~{\rm au}$  (median: 31 au). RMS values lie between  $\sim 0.5{-}47~{\rm K}$  (median: 3.4 K) when scaled for a channel width of  $100~{\rm m\,s^{-1}}$ .

To assess if combining re-imaged and archival products affects our results, we compared the re-imaged data sets with the archival products for the same data set. We find that the Keplerian fit (see Sect. 4.4.2) is not significantly affected. The detection of extended (over several beams) substructures, such as spirals or the non-detection of features, is also not affected. Only tentative features are sometimes only visible in the re-imaged data. Some examples for this test are shown in Fig. 4.D.1 in the Appendix: while clear spirals are found in both the re-imaged and archival product data of UX Tau A, a tentative spiral in the brightness temperature of HD 135344B and a tentative spiral (or arc) in the kinematics of J1604 are only visible in the re-imaged data. RXJ 1615, on the other hand, shows no clear spirals or arcs in both data products.

Several discs in our sample are affected by cloud absorption, namely AB Aur, HD 142527, HD 97048, HP Cha, IP Tau, IRS 48, PDS 99, SR 21, Sz 91, and SZ Cha. We masked the regions affected by this in the calculations of the radial profiles (Sect. 4.3.3) and brightness temperature residuals (Sect. 4.4.1). For some of the targets, we analysed additional CO isotopologues, which are listed with the data properties in the Appendix in Table 4.E.1. Our main lines for analysis (Table 4.2) are based on their brightness as well as the spatial and spectral resolution of the observation. A few of our targets have already been analysed with the same techniques, as explained in Sect. 4.4 (CQ Tau, Wölfer et al. 2021; HD 100453 Rosotti et al. 2020a; and TW Hya Teague et al. 2019b), but they are included in this work for comparison.

Table 4.1: Stellar properties, outer disc inclination, and dust cavity radius of the disc sample studied in this work.

Object	(pc)	Spectral type	$T_{\rm eff}$ (K)	$L (L_{\odot})$	$M_*~(M_\odot)$	i (°)	Classification	Dust cavity (au)	$\operatorname{Ref.}^{(a)}$
AA Tau	137	K7	4350	1.1	0.68	59	$\operatorname{LLS}$	44	1
ABAur	163	A0	9520	65.1	2.56	23	Herbig	156	Н
CQ Tau	163	F2	0689	10.0	1.63	35	Herbig	20	П
CS Cha	176	K2	4780	1.9	1.4	$\infty$	$\Gamma$	37	П
DM Tau	145	M2	3580	0.2	0.39	35	$_{ m LLS}$	25	П
DoAr44	146	K2	4780	1.9	1.4	20	$\Gamma$	40	П
GG Tau	140	$ m K7{+}M0$	4060	1.6	0.66	36	$_{ m LLS}$	224	П
$_{ m GMAur}$	160	K5	4350	1.0	1.01	53	$_{ m LLS}$	40	П
$\mathrm{HD}100453$	104	F0	7200	6.2	1.47	30	Herbig	30	П
$\mathrm{HD}100546$	110	A0	9520	25.0	2.13	42	Herbig	27	$\vdash$
$\mathrm{HD}135344\mathrm{B}$	136	F5	6440	2.9	1.51	12	Herbig	52	П
$\mathrm{HD}139614$	134	A9	7750	0.9	1.57	18	Herbig	1	2
$\mathrm{HD}142527$	157	${ m F6+M5/M6}$	0989	6.6	$1.69{+}0.26$	27	Herbig	185	1,3
$HD\ 169142$	114	A5	8200	8.0	1.65	12	Herbig	26	$\vdash$
HD34282	312	A0	9520	10.8	2.11	59	Herbig	87	П
$\mathrm{HD}97048$	185	A0	9520	30.0	2.17	41	Herbig	63	П
HP Cha	160	K7	4060	2.4	0.95	37	$_{ m LLS}$	50	Π
IP Tau	131	M0	3850	9.0	0.54	45	$_{ m LLS}$	25	Π
IRS 48	134	A0	9520	17.8	1.96	20	Herbig	83	$\vdash$
J1604.3 - 2130	150	K3	4780	0.7	1.1	9	SLL	87	$\vdash$
LkCa15	159	K2	4730	1.3	1.32	55	$\operatorname{SLL}$	92	Π
MWC758	160	A7	7850	14.0	1.77	21	Herbig	62	$\vdash$
PDS70	113	K7	4060	0.3	0.8	52	$_{ m LLS}$	74	$\vdash$
PDS99	155	K6	4205	1.1	0.88	55	$\Gamma$	56	1
RXJ1615.3-3255	156	K7	4100	9.0	0.73	47	LTS	1	2

Table 4.1 continued.

Object $d$ (pc)	d (pc)	Spectral type	$T_{\rm eff}$ (K)	$L$ $(L_{\odot})$	$M_*~(M_\odot)$	i (°)	Classification	Dust cavity (au)	$\operatorname{Ref.}^{(a)}$
RXJ1852.3-3700	146	K2	4780	9.0	1.05	30	$_{ m LLS}$	49	1
$\mathrm{RY}\mathrm{Lup}$	159		4780	1.9	1.4	29	$\Gamma$	69	П
RY Tau	175	G2	2860	15.0	2.25	65	$\operatorname{LLS}$	27	$\vdash$
$\mathrm{SR}21$	138		5770	11.0	2.12	16	$\operatorname{LLS}$	26	$\vdash$
$\operatorname{Sz} 91$	159		3850	0.2	0.54	45	$\Gamma$	98	$\vdash$
$\operatorname{SZCha}$	190		5100	1.7	1.45	47	$\Gamma$	1	2
T  Cha	107		5570	1.3	1.12	73	$\Gamma$	34	$\vdash$
${ m TWHya}$	09		4205	0.3	0.81	7	SLL	2	$\vdash$
$\operatorname{UX}\operatorname{Tau}\operatorname{A}$	140	G8	5570	2.5	1.4	40	SLL	31	$\vdash$
V1247 Ori	400		7200	15.0	1.82	30	Herbig	64	$\vdash$
m V4046Sgr	72	$_{ m K7+K5}$	4060	0.5	0.9 + 0.85	34	$\Gamma$	31	1,4

disc inclination are taken from (1) Francis & van der Marel (2020) where all original references for the spectral type can be Notes. (a) Unless indicated otherwise, data for spectral type, distance, effective temperature, stellar luminosity, stellar mass, and found. The distances are according to Gaia Collaboration et al. (2018). (2) Bohn et al. (2022), (3) Claudi et al. (2019), (4) Rosenfeld et al. (2012). The radius of the dust cavity was determined by Francis & van der Marel (2020).

Table 4.2: Characteristics of the ALMA line data for the main lines of this analysis.

Object	Line	Project ID	Beam (")	LAS (")	$\Delta v \; (\mathrm{km}  \mathrm{s}^{-1})$	$RMS (mJy beam^{-1})$	Cube source $^{(a)}$	Ref.
AA Tau	$^{13}$ CO 3-2	2015.1.01017.S	0.28x0.22	8.0	0.11	13.5	A	
ABAur	$^{13}$ CO 3-2	2012.1.00303.S	$0.37\mathrm{x}0.23$	7.2	0.2	6.2	$\mathrm{P/PC}$	1
CQ Tau	$^{12}CO\ 2-1$	2013.1.00498.S	0.12x0.1	5.3	0.5	1.2	P/PC	2
		2016.A.00026.S		2.9				
		2017.1.01404.S		2.7				
CSCha		2017.1.00969.S	$0.1 \times 0.07$	2.4	0.11	4.2	A	
DM Tau		2016.1.00724.S	$0.86 \times 0.8$	10.5	0.08	17.6	A	
DoAr 44		2012.1.00158.S	0.25x0.19	3.2	0.5	13.7	$\mathrm{P/PC}$	ဘ
$\operatorname{GG}\operatorname{Tau}$		2018.1.00532.S	0.34 x 0.27	9.7	0.08	2.6	A	
${ m GMAur}$		2018.1.01055.L	$0.15\mathrm{x}0.15$	3.6 - 44.1	0.2	2.8	$\mathrm{P/PC}$	4, 5
$\mathrm{HD}100453$		2017.1.01424.S	$0.05\mathrm{x}0.05$	1.3	0.42	1.0	$\mathrm{P/PC}$	9
$\mathrm{HD}100546$		2016.1.00344.S	0.08x0.06	1.1/2.7	0.5	1.2	$\mathrm{P/PC}$	7
$\mathrm{HD}135344\mathrm{B}$		2012.1.00158.S	$0.26\mathrm{x}0.21$	3.1	0.24	19.1	$\mathrm{P/PC}$	3
$\mathrm{HD}139614$		2015.1.01600.S	0.77x0.55	8.4	0.4	26.5	$\mathrm{P/PC}$	$\infty$
$\mathrm{HD}142527$		2015.1.01353.S	$0.28 \times 0.26$	3.9	0.09	2.5	A	
$\mathrm{HD}169142$	$^{12}CO$ 2-1	2015.1.00490.S	$0.18 \mathrm{x} 0.13$	4.2	0.05	1.2	$\mathrm{P/PC}$	6
$\mathrm{HD}34282$		2013.1.00658.S	$0.26 \times 0.2$	5.1/9.7	0.2	8.2	$\mathrm{P/PC}$	10
$\mathrm{HD}97048$		2016.1.00826.S	0.11x0.07	1.8/4.4	0.12	3.8	$\mathrm{P/PC}$	11
HPCha		2016.1.00583.S	$0.3 \times 0.21$	6.2	0.63	3.7	A	
IP Tau		2013.1.00163.S	0.24x0.21	3.2	1.0	5.5	$\mathrm{P/PC}$	12
IRS48		2013.1.00100.S	0.19x0.13	1.4-3.5	0.24	8.3	$\mathrm{P/PC}$	13
J1604	$^{12}CO$	2015.1.00888.S	0.23x0.19	3.3/6.7	0.21	7.1	$\mathrm{P/PC}$	14
LkCa 15	$^{12}CO$	2018.1.01255.S	0.41x0.29	9.2	0.04	0.9	$\mathrm{P/PC}$	15
$\overline{\mathrm{MWC}}$ 758	$^{13}$ CO	2012.1.00725.S	0.19x0.16	5.0	0.11	8.9	$\mathrm{P/PC}$	16
PDS70	$^{12}CO\ 3-2$	2017.A.00006.S	0.11x0.1	2.3	0.42	1.1	$\mathrm{P/PC}$	17

**Table 4.2** continued.

Object		Project ID	Beam (")	LAS (")	LAS (") $\Delta v  (\mathrm{km  s}^{-1})$	$RMS (mJy beam^{-1})$	Cube source $^{(a)}$	Ref.
PDS99	$^{12}CO\ 2-1$	2015.1.01301.S	$0.3 \times 0.22$	4.9	0.16	8.3	A	
RXJ1615		2012.1.00870.S	$0.3 \times 0.23$	3.2/6.5	0.21	14.1	P/PC	18
RXJ1852		2018.1.00689.S	$0.16 \times 0.12$	1.8	0.63	4.3	Ā	
m RYLup		• •	0.22x0.17	2.71	0.85	4.0	P/PC	19
$\operatorname{RY}$ Tau		2013.1.00498.S	$0.28 \times 0.16$	1.67	0.5	9.1	Ā	
$\mathrm{SR}21$		2018.1.00689.S	0.14x0.12	1.71	0.64	4.8	A	
$\operatorname{Sz}91$		2012.1.00761.S	$0.17 \mathrm{x} 0.13$	1.36	0.2	11.8	A	
$\operatorname{SZCha}$		2013.1.01075.S	0.82x0.43	3.70	0.5	26.2	P/PC	12
TCha		2017.1.01419.S	0.24x0.17	2.55	0.32	9.0	Ā	
${ m TWHya}$		2015.1.00686.S	0.14x0.13	0.37	0.25	3.5	$\mathrm{P/PC}$	20
		2016.1.00629.S		1.3/6.0				
$\mathrm{UX}\mathrm{Tau}\mathrm{A}$		2015.1.00888.S	0.2x0.16	2.41	0.21	3.4	P/PC	21
V1247 Ori	$^{12}CO\ 3-2$	2016.1.01344.S	$0.05 \times 0.03$	0.86	1.0	2.0	P/PC	22
m V4046Sgr		2016.1.00724.S	0.41x0.29	4.48	0.08	6.6	A	

References. (1) van der Marel et al. (2021); (2) Wölfer et al. (2021); (3) van der Marel et al. (2016); (4) Öberg et al. (2021); (5) Notes. (a) P/PC: re-imaged data cube. Public data or obtained via private communication, A: archival data product.

Huang et al. (2021); (6) Rosotti et al. (2020a); (7) Pérez et al. (2020); (8) Stapper et al. in prep.; (9) Yu et al. (2021); (10) van (2018); (15) Leemker et al. (2022); (16) Boehler et al. (2018); (17) Keppler et al. (2019); (18) Perez et al. in prep.; (19) Qian et der Plas et al. in prep.; (12) Pinte et al. (2019); (12) Bohn et al. (2022); (13) van der Marel et al. in prep.; (14) Mayama et al. al. in prep.; (20) Huang et al. (2018); (21) Ménard et al. (2020); (22) Kraus et al. (2017)

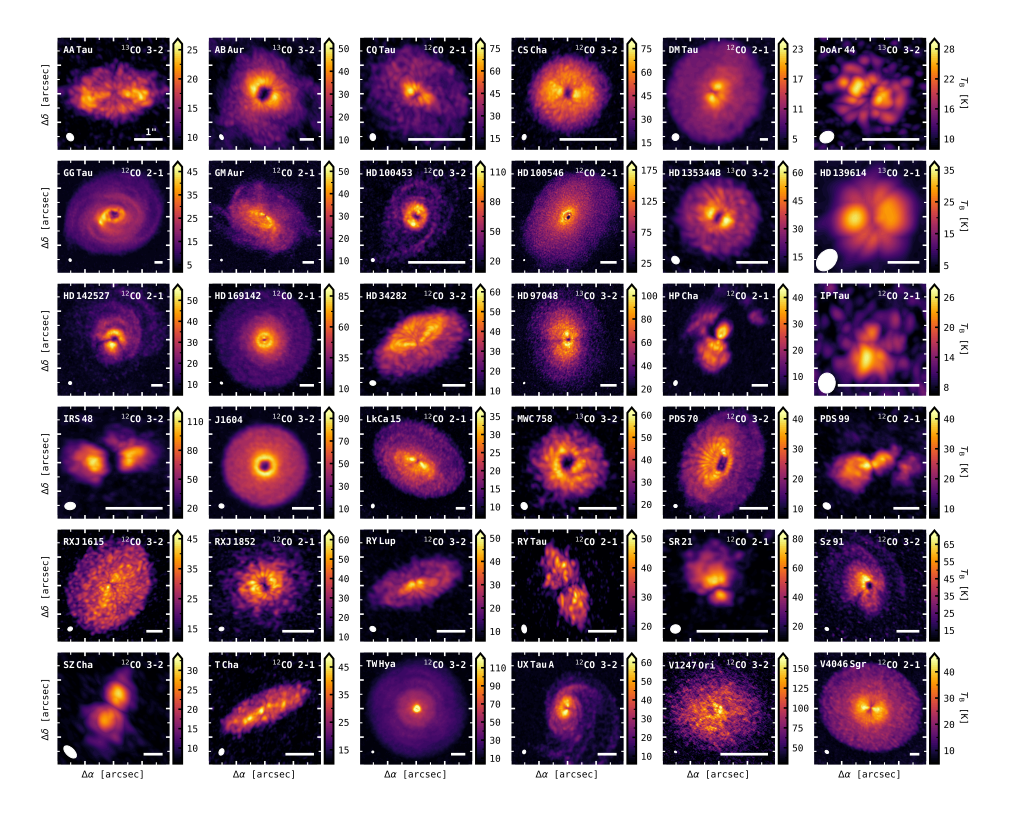


**Figure 4.1:** Peak brightness temperature maps of the gas emission in our targets, shown for the main CO lines used in this analysis. The conversion from peak intensity to units of Kelvin was done with the Planck law. The circle and bar in the bottom left and bottom right corner of each panel indicate the beam and a 1" scale, respectively.

## 4.3 Observational results

## 4.3.1 Brightness temperature

In Fig. 4.1 we present the peak brightness temperature maps (continuum subtracted) for the main CO lines (mostly <sup>12</sup>CO and some <sup>13</sup>CO). Maps for the additional lines can be found in Figs. 4.E.1 and 4.E.2 in the Appendix. The maps presented in Fig. 4.1 are shown again in Fig. 4.A.1 with overlaid continuum images, illustrating that for most targets the dust disc (millimetre-sized grains, B6 and B7) is substantially smaller than the gas disc. This can readily be explained by radial drift processes and/or by the difference between dust and gas opacities (Facchini et al. 2017; Trapman et al. 2019).

To compute the peak intensity maps, we used the standard moment eight implementation in the BETTERMOMENTS code (Teague & Foreman-Mackey 2018) and then converted from flux density units to units of Kelvin with the Planck

law. No masking was applied in the computation of the maps. The brightness temperature traces a combination of kinetic gas temperature and column density, with the optically thick lines mostly measuring the temperature while the more optically thin lines mostly trace the column density. In this context, the observed gas temperatures of  $\sim 30\,\mathrm{K}$  up to  $\sim 200\,\mathrm{K}$  are as expected in the upper disc layers (see e.g., Bruderer 2013; Bruderer et al. 2014; Leemker et al. 2022). As discussed below, some of the discs show interesting features in their peak brightness temperature. Very massive companions are clearly observable from the peak brightness temperature due to their ability to induce spirals which are prominent enough to be observed with this data quality. Clear spiral structures can be discerned in GG Tau, HD 100453, HP Cha, and UX Tau A. GG Tau is (at least) a quadruple star system surrounded by a massive disc, with the substructures likely tracing stardisc or planet-disc interactions (Leinert et al. 1991; Dutrey et al. 2014a; Phuong et al. 2020a). HD 100453 and UX Tau A are also known to have stellar companions that are responsible for the observed spirals (Rosotti et al. 2020a; Ménard et al. 2020). HP Cha is affected by cloud absorption on the blueshifted side, but the extended (redshifted) structure suggests interactions with the environment such as infalling material from a streamer or a fly-by. Even though the disc around V4046 Sgr is also known to be circumbinary, no clear substructures can be seen. The reason for this is that the two stars in the system are orbiting each other at a small distance (< 1 au, 2.4 d, Stempels & Gahm 2004), acting similar to a single gravitational point source on much larger scales.

Indications of spirals are visible in CQ Tau, where one side of the disc is substantially brighter, representing the anchoring point of the spiral (see Wölfer et al. 2021) as well as in HD 135344B and TW Hya. For HD 135344B, similar spiral features have been found by Casassus et al. (2021) in <sup>12</sup>CO 2-1 data. Other discs such as HD 142527 (in all CO isotopologues, Casassus et al. 2015; Garg et al. 2021; Yen & Gu 2020) or Sz 91 show arc-like azimuthal asymmetries. Tsukagoshi et al. (2019) explain the arc-like structure in Sz 91 with a flared disc, showing emission from the front and the back side, in combination with a dust ring.

In a couple of maps – for example of AB Aur, CQ Tau, or MWC 758 – symmetric dimmed regions are visible. Such features are commonly linked to the presence of a misaligned inner disc, casting a shadow over the outer disc (e.g., Marino et al. 2015; Facchini et al. 2018). Beam dilution effects can, however, cause artificial features along the minor axis (see example of CQ Tau in Wölfer et al. 2021), thus caution should be taken when interpreting these under-brightnesses. The misalignment hypothesis has recently been tested by Bohn et al. (2022) for a sub-sample of our discs by comparing the position angle and inclination of the inner disc measured with VLTI/GRAVITY and the outer disc measured with ALMA. Significant misalignments are found for CQ Tau, HD 100453, HD 142527, HD 34282, RY Lup, and V1247 Ori. Francis & van der Marel (2020) also find misalignments from ALMA inner disc images, which are significant for eight sources in either position angle or inclination (AB Aur, GG Tau, HP Cha, MWC 758, PDS 70, SR 24 S, TW Hya, and V4046 Sgr). In Fig. 4.2, some examples are given for the different features that can be observed in the brightness temperature. We note that arcs can also be seen as part of a spiral. In this work we identify spirals as structures covering a larger

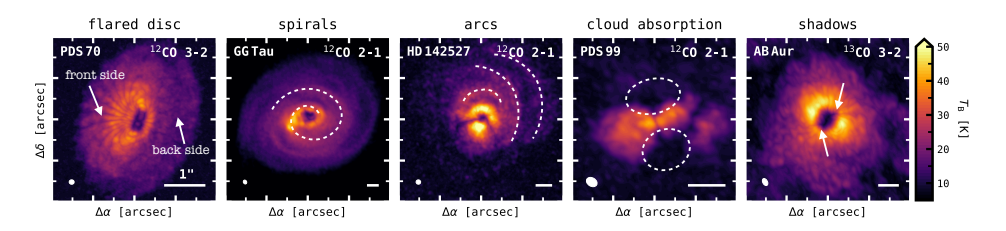


**Figure 4.2:** Examples of the different features seen in the brightness temperature of our sources. The circle and bar in the bottom left and bottom right corner of each panel indicate the beam and a 1" scale, respectively.

range of radii, while arcs are mostly observed at one radius.

To uncover small substructures in the brightness temperature structure, we further analyse these maps in Sect. 4.4.1 by subtracting azimuthally symmetric brightness temperature profiles from the data.

#### 4.3.2 Rotation velocity

In Fig. 4.3 we present the kinematics of our targets, again showing the main lines, while the additional lines can be found in the Appendix in Figs. 4.E.3 and 4.E.4. To compute the line-of-sight velocity of the gas, we used the quadratic method implemented in the BETTERMOMENTS package: a quadratic function is fitted to the brightest pixel in the spectrum as well as the two neighbouring pixels to find the centroid of the line in pixel coordinates. To reduce the noise at the disc edge, we applied a masking for regions below a certain signal-to-noise ratio (S/N). The magnitude of this clipping was obtained via inspection of each individual map, ranging between  $2\sigma$  to  $5\sigma$ .

Even though the spiral features are not as prominent in the kinematics as in brightness temperature maps, they are still observable in GG Tau, HD 100453, HP Cha, and UX Tau A. CQ Tau, HD 135344B, and TW Hya show indications of spirals in the brightness temperature, in the kinematics these indications are only present for TW Hya. CQ Tau, however, shows twisted kinematics in the centre that resemble a warp, but are likely caused by the spiral structure (Wölfer et al. 2021). Clearly twisted kinematics can also be seen in the centre of HD 142527, for which several indications of a warped disc have been found (Marino et al. 2015; Casassus et al. 2015; Bohn et al. 2022).

For several discs with higher inclinations, the vertical structure becomes visible in the isovelocity curves bending away from the semi-major axis in one direction (e.g., AA Tau, GM Aur, HD 97048, LkCa 15, PDS 70, RY Lup, T Cha, and V1366 Ori). Fitting for this structure can be used to determine the flaring and scale height of the disc (e.g., Casassus & Pérez 2019; Teague et al. 2019a). Other more face-on or inclined, yet less elevated discs show a dipole morphology that is symmetric about the semi-major axis (e.g., AB Aur, CS Cha, HD 135344B, HD 139614, TW Hya, and V4046 Sgr).

To reveal possible deviations from Keplerian rotation that may be indicative of

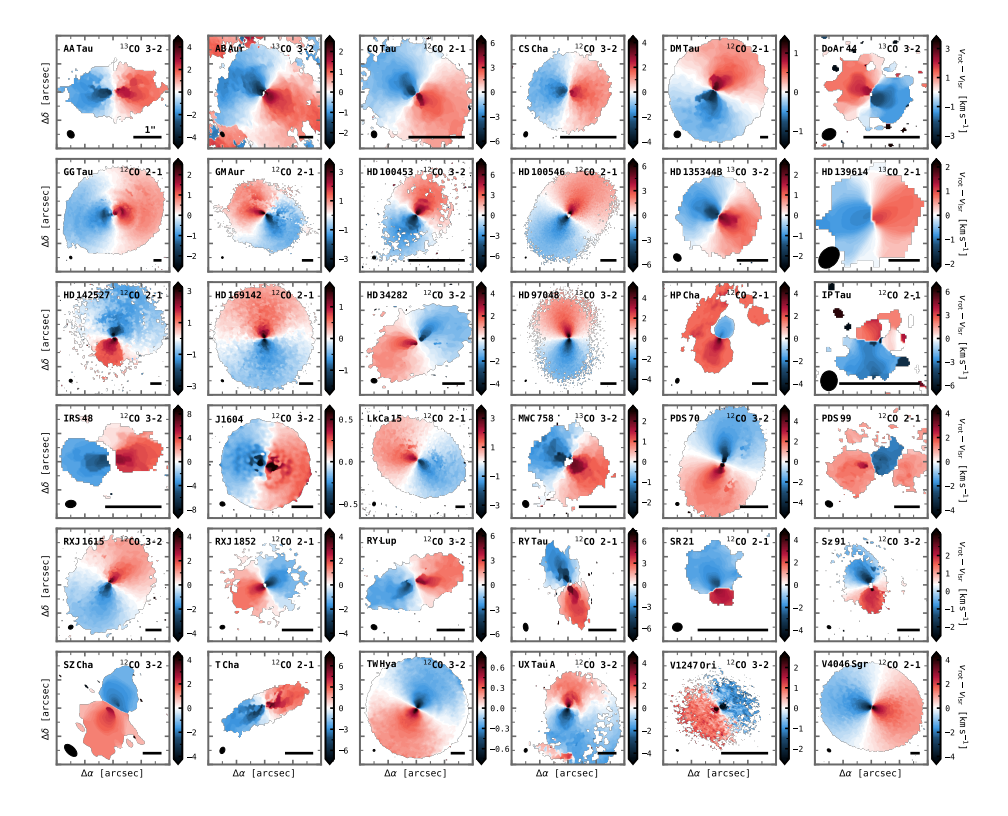


**Figure 4.3:** Rotation velocity maps of the gas emission in our targets, shown for the main CO lines used in this analysis. The maps were computed with BETTERMOMENTS. The circle and bar in the bottom left and bottom right corner of each panel indicate the beam and a 1" scale, respectively.

the presence of companions, we attempt to fit a Keplerian model to the rotation velocity of the discs in Sect. 4.4.2 assuming thin and thick disc geometries.

## 4.3.3 Radial profiles

In Fig. 4.4, the radial peak intensities are displayed for the different CO lines (coloured lines) as well as the millimetre continuum (black lines). These curves were calculated by azimuthally averaging the peak intensities for radial annuli of an equal width, using the GOFISH package (Teague 2019). By default, the widths of the annuli in this package are given as one-fourth of the beam major axis. For the computation we assumed the geometries (thin or thick disc) obtained from the fitting of the rotation maps (see Sect. 4.4.2). For both geometries we recovered similar radial profiles (due to similar fits, see discussion in Sect. 4.4.2) and thus the curves are only shown for the thin disc geometry in Fig. 4.4. All profiles are plotted normalized to the peak value. The uncertainties, shown as shaded regions, correspond to the standard deviation per annulus divided by the square root of

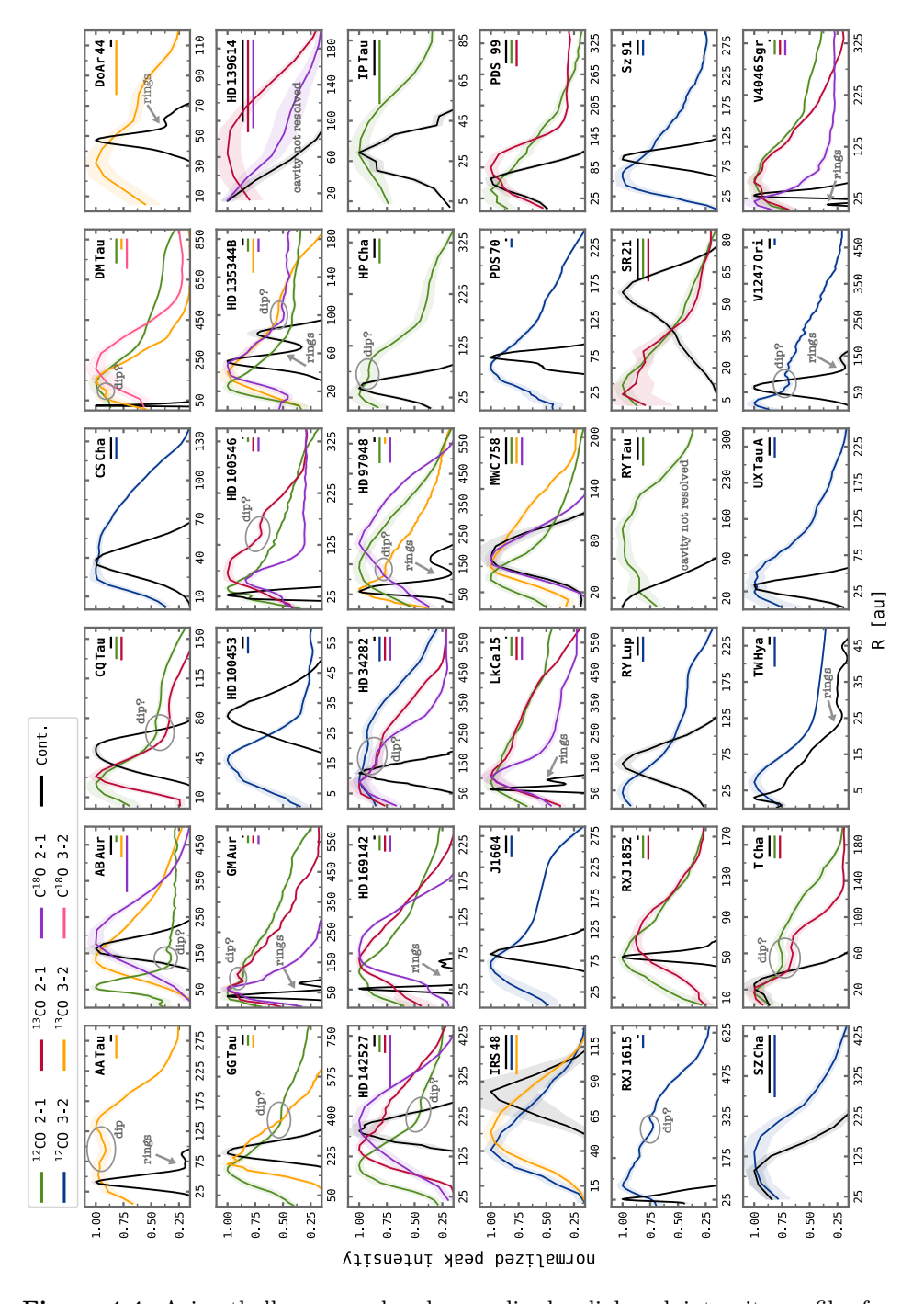


**Figure 4.4:** Azimuthally averaged and normalized radial peak intensity profiles for the different CO lines (coloured lines) and continuum emission (black lines). The major beam of each observation is indicated by the bars in the top right corner. Some features of the profiles are annotated in the individual panels.

106 4.4. ANALYSIS

the number of independent beams in the annulus. Some discs in our sample are affected by cloud absorption, which can result in an artificially lower brightness temperature and a larger azimuthal scatter. We therefore excluded the affected azimuthal angles from our calculation. The beam size of the continuum and lines is indicated by a coloured bar in each panel. The interpretation of radial profiles depends on the resolution. Given the inhomogeneity of our sample in that regard, the trends reported below may be subject to change with higher and comparable resolutions. The main features of the profiles are annotated in the individual panels of Fig. 4.4.

The radial profiles can be used to estimate the size of the cavity (steep emission drop). In this context, it is important to note that artificial cavities can be created in the peak intensity, depending on the beam size. Near the star the emission is less extended than the beam size and during the beam convolution the intensity gets diluted over the full extent of the beam, hence the peak intensity decreases. When studying the inner disc, it is therefore important to look at the velocity-integrated intensity, which is less affected by this issue. However, for the integrated intensity, there may be contributions from the back side of the disc (Rab et al. 2019). The radial profiles for the integrated intensity are shown in the Appendix in Fig. 4.F.1.

The measured brightness temperature is also affected by the subtraction of the continuum (except for HD 97048, all data are continuum subtracted). For optically thick lines, which absorb part of the underlying continuum, line emission may be removed when subtracting the continuum, leading to artificial temperature drops (e.g., Weaver et al. 2018; Rosotti et al. 2021; Bosman et al. 2021). Since in this work we are mostly interested in substructures rather than obtaining a robust measurement of the temperature, we do not expect this effect to significantly affect our results.

As is visible in Fig. 4.4 (and Fig. 4.F.1), the CO emission peaks inside the dust cavity for most discs, which is as expected from previous work (Bruderer 2013; van der Marel et al. 2016). For a few discs, such as HD 139614, the inner dust cavity is not resolved due to limited resolution. The radial profiles can further show dips or wiggles, especially in the dust indicating ring structures and depleted regions. It is important to note that it is also possible that instead of a dip, an enhanced desorption of CO ices by increased UV or a temperature inversion in the outer disc (more optically thin) at the edge of the continuum can result in an enhancement of gas emission (e.g., Cleeves et al. 2016; Facchini et al. 2017).

## 4.4 Analysis

## 4.4.1 Brightness temperature structure

To uncover possible substructures in the brightness temperature, we constructed an azimuthally symmetric model with GOFISH and subtracted this model from the data. The package computes an azimuthally averaged radial profile for a given geometry (compare Sect. 4.3.3) and then projects it onto the sky to create an azimuthally symmetric model. For the disc geometry, we used the results for the thin and (if available) the vertically extended thick disc from the kinematics

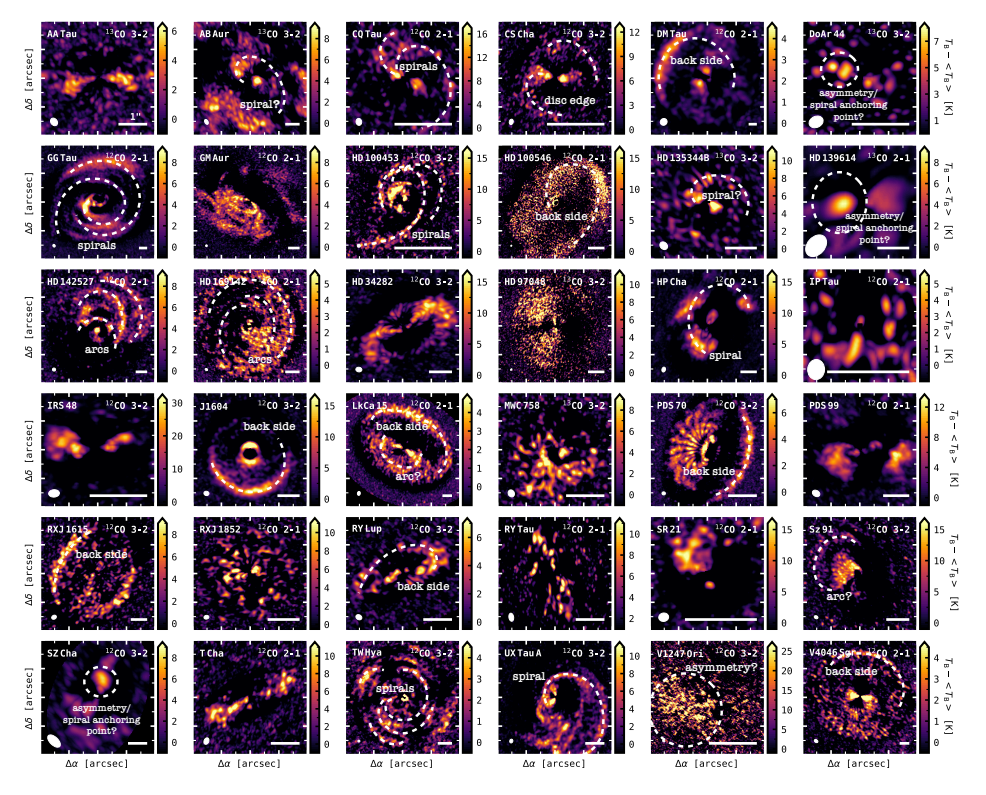


**Figure 4.5:** Brightness temperature residuals obtained with GOFISH, shown for the main CO lines used in this analysis and for a geometrically thin disc approximation. The circle and bar in the bottom left and bottom right corner of each panel indicate the beam and a 1" scale, respectively. The main features are annotated.

modelling described in Sect. 4.4.2. The angles affected by cloud absorption were again excluded from the calculation. The resulting residuals are presented in Fig. 4.5 for the geometrically thin disc and in the Appendix for the geometrically thick disc models (Fig. 4.B.1). The colour scale has been adapted such that regions with hotter temperatures than the model are highlighted. In this work we are mostly interested in the general occurrence of features such as spirals and therefore this choice was made to help the readability of the plot. Residuals for the other CO lines can also be found in the Appendix. The main features are annotated in the individual panels and further discussed in Sect. 4.5.

## 4.4.2 Velocity structure

To analyse the gas kinematics of our sample, we used the EDDY code (Teague 2019) to fit a Keplerian profile

$$v_{\rm rot}(r,\phi) = \sqrt{\frac{GM_*}{r}} \cdot \cos\phi \cdot \sin i + v_{\rm LSR},$$
 (4.1)

108 4.4. ANALYSIS

with  $(r,\phi)$  being the deprojected cylindical coordinates, i the inclination of the disc, and  $v_{\rm LSR}$  the systemic velocity, to the rotation maps shown in Fig. 4.3. To deproject the sky-plane coordinates (x,y) into the midplane cylindrical coordinates  $(r,\phi)$ , the disc centre  $(x_0,y_0)$ , i, and the disc position angle PA were used. The latter is measured between the north and the redshifted semi-major axis in an easterly direction. As a first step, the starting positions of the free fit parameters were optimized with scipy.optimize and their posterior distributions were estimated using the Markov chain Monte Carlo (MCMC) sampler.

In addition to the model for a geometrically thin disc, EDDY also includes the possibility to fit for the vertical structure of the disc. To parameterize the emission layer, we chose a simple model of a flared disc described by

$$z(r) = z_0 \cdot \left(\frac{r}{1''}\right) \cdot r^{\psi},\tag{4.2}$$

where  $z_0$  describes the elevation and  $\psi$  the flaring angle of the emission surface.

In the modelling process, we fixed the object's distance and stellar mass, taken from the literature, and fitted for the disc centre  $(x_0, y_0 \in [-0.5, 0.5])$ , systemic velocity  $(v_{LSR} \in [v_{min}(\text{data}), v_{max}(\text{data})])$ , inclination  $(i \in [-90^\circ, 90^\circ])$ , and disc position angle  $(PA \in [-360^\circ, 360^\circ])$  as well as surface elevation  $(z_0 \in [0, 5])$  and flaring angle  $(\psi \in [0, 5])$  in the geometrically thick disc approximation. We also conducted runs where the inclination was fixed instead of the stellar mass and where both the inclination and the stellar mass were left as free parameters. Overall the results are very similar for these different cases and in the following we only show the results for the models where the stellar mass was fixed.

For most targets we downsampled the data by a factor of 2–4 before fitting. We fitted for the whole disc, choosing an outer radius depending on the disc size to exclude possible noise at the disc edge and an inner radius of twice the beam major axis to exclude regions that are strongly affected by beam smearing. For a few cases, where the beam is very large, we slightly reduced this inner radius to ensure a reasonable number of pixels to fit. For all models we used 100 walkers, 8000 steps to burn in, and 2000 additional steps to sample the posterior distribution function and assumed flat priors that were allowed to vary over a wide range. The uncertainties of the posterior distributions represent the 16th to 84th percentiles about the median value. The uncertainties on the kinematics, computed with BETTERMOMENTS, were included in the fit and are shown in Fig. 4.C.1. They mostly lie well below the channel width, but they increase in the central regions due to beam smearing.

While most models converged rapidly within a couple 100 steps, none of the models for HP Cha converged. Furthermore, the models considering the vertical structure of the disc – despite rapidly converging – often do not match the bending of the isovelocity curves clearly seen in the data of the higher-inclination discs and return substantially smaller values for the elevation and flaring than expected. We tried both orientations of the inclination (positive and negative) in this context. For highly inclined sources, the back side becomes prominently visible, resulting in a quadrupole morphology. However, this was fit with a dipole morphology and therefore the best fit lies between the two lobes of the quadrupole morphology,

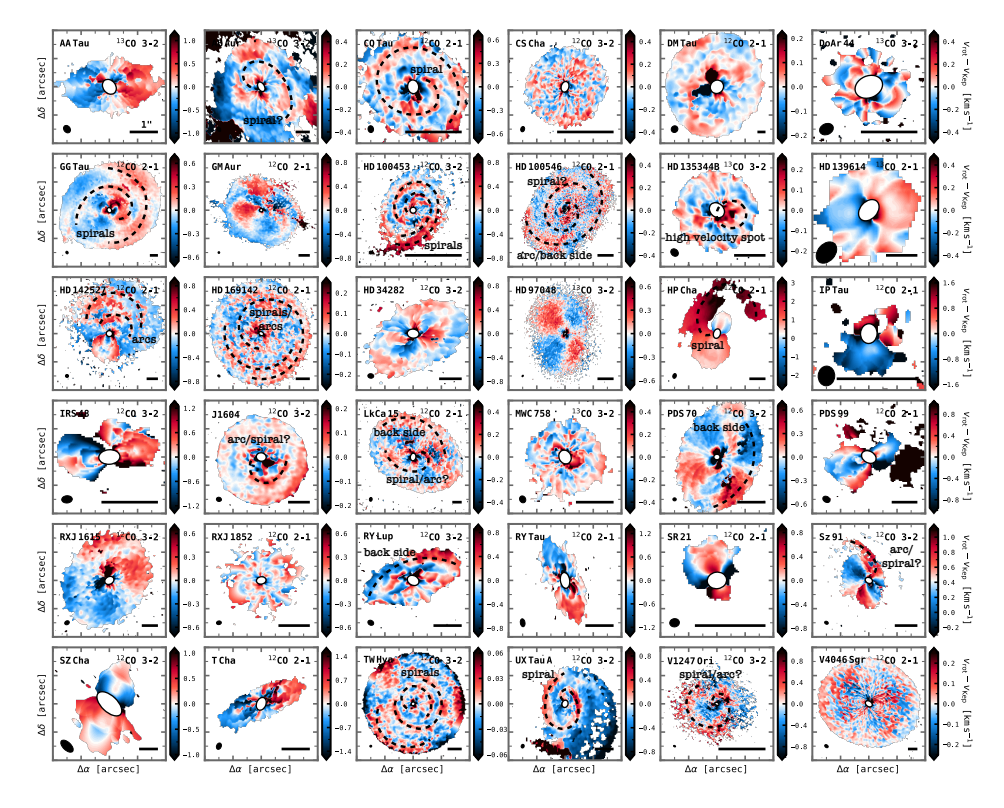


**Figure 4.6:** Rotation velocity residuals obtained with EDDY, shown for the main CO lines used in this analysis and for a geometrically thin disc approximation. The circle and bar in the bottom left and bottom right corner of each panel indicate the beam and a 1" scale, respectively. The main features are annotated.

representing the average of the front and back side of the disc. The residuals of these models thus resemble those of the flat disc (see Figs. 4.6 and 4.B.1). Higher spectral and spatial resolution data and individual modelling of the two disc sides (front and back) may be required to find a better fit for the vertical structure (e.g., directly from the channel maps).

In Fig. 4.6, the residuals after subtraction of the Keplerian model from the data are shown for the geometrically thin disc approximation. The residuals of the vertically extended disc approximation of the main CO lines are presented in Fig. 4.B.1. Again, the residuals for the other CO lines can be found in the Appendix. In the plots we have masked out disc regions inside of twice the beam, since these are strongly affected by beam smearing and not included in the fit. The main features are again annotated in the individual panels and further discussed in the following section. Same as for the brightness temperature residuals, we have marked the substructures found in the positive residuals. While it is interesting to study both the positive and negative residuals, the interpretation of these structures is not straightforward and a lot of effort is currently put into

110 4.5. DISCUSSION

understanding the different patterns, which will be part of upcoming works. In contrast to that, this work aims to compare the different substructures found in the gas of circumstellar discs that may be indicative of embedded planets.

#### 4.5 Discussion

The residuals presented in Figs. 4.5 and 4.6 show various features that are annotated in the different panels. For the discs that show very clear substructures (see Sect. 4.5.1), the different maps and radial profiles are collected again in Fig. 4.7.

For several higher-inclination discs, the vertical structure is still clearly visible in the residuals in form of a butterfly-like pattern even after subtraction of a geometrically thick disc model (e.g., AA Tau, HD 34282). As previously mentioned, most of these fits returned only slightly elevated emission surfaces and are not able to reproduce the actual vertical structure of the disc. For these geometrically thick disc models, still only a single side of the disc has been modelled; whereas, for the highly inclined discs, both the front and back sides are visible. An approach modelling both sides independently (such as used in the DISCMINER, Izquierdo et al. 2021) would be needed to avoid this problem. Connected to that, in a few cases, arc features can be seen at the disc edge, which result from looking into the back side of the disc (e.g., J1604, LkCa 15, and PDS 70).

In Table 4.3 we list some features that may be indicative of interactions between the disc and planets and/or stellar companions. Here, a green check mark stands for the detection of a feature, a red cross identifies a non-detection, and brackets indicate a tentative detection. Especially if several features are observed in the same disc, this is a strong indication that we are tracing embedded planets or companions. As a deep gas cavity, we have marked cases where a clear drop is seen in the radial profile of the peak and integrated intensity for at least the more optically thin lines that tend to trace the column density. In a few cases, such as LkCa 15 or HD 34282, no steep drop is discerned, but the gas cavity is very extended and better data are needed to confirm if a deep cavity is present (Leemker et al. 2022). In this work we do not investigate the presence of kink features and thus these are missing as a possible planet signpost in Table 4.3. While Pinte et al. (2020) report the detection of such azimuthally located features in about half of the discs in the DSHARP programme (Andrews et al. 2018), more data are needed to confirm the robustness of such claims and it is difficult to draw conclusions on the presence of kinks in our sample, given the inhomogeneity of spatial and spectral resolutions. Furthermore, the interpretation of kink features is not straightforward as they can be caused by a gap or density substructure rather than a planet (Izquierdo et al. 2021). More detailed studies (beyond the scope of our work) of a homogenous data set at high resolution are needed to test for such scenarios. In the following, we describe the observed structures in more detail.

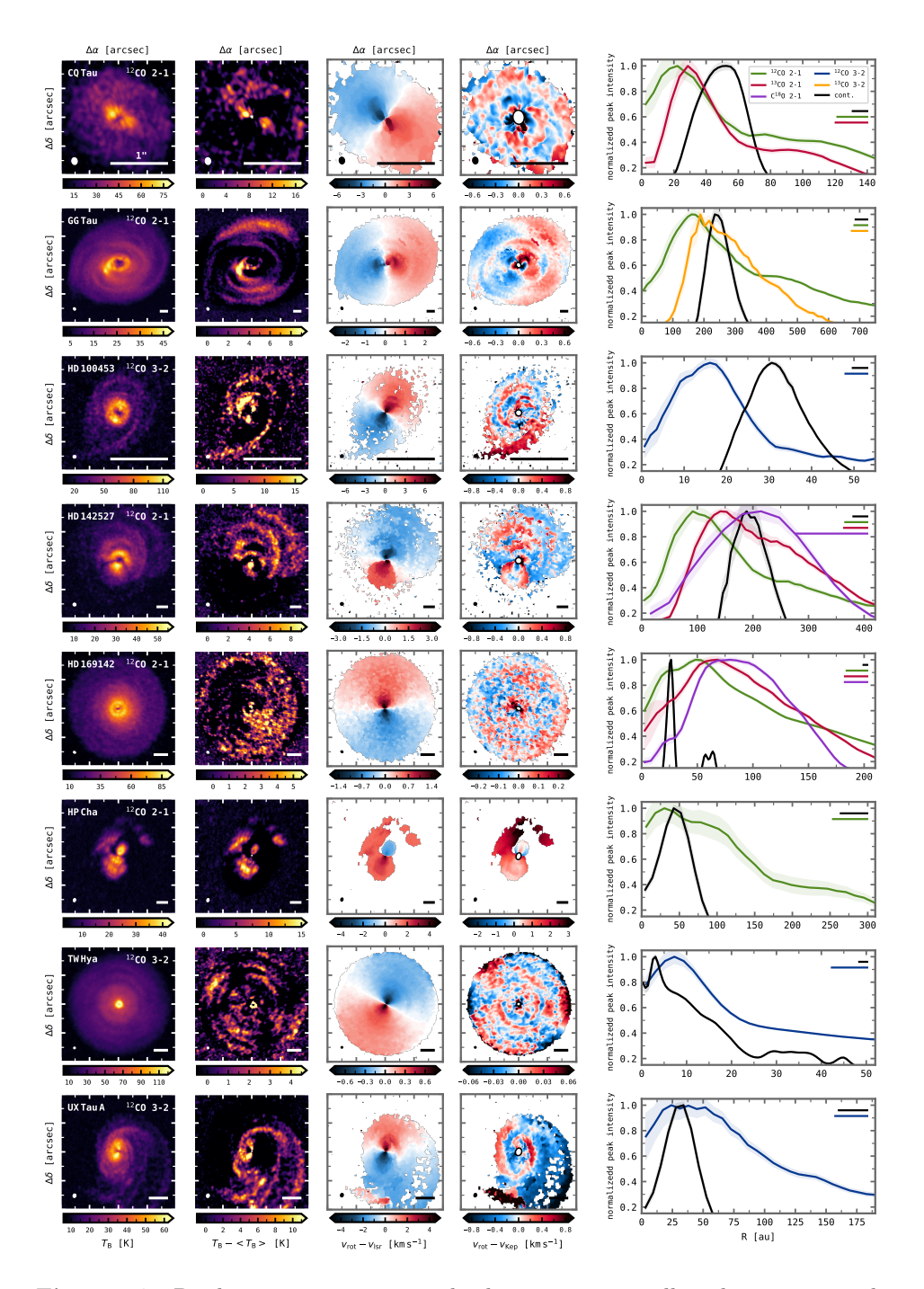


**Figure 4.7:** Brightness temperature and velocity maps as well as their corresponding residuals and radial profiles, shown for the eight targets with the clearest substructures. The circle and bar in the bottom left and bottom right corner of the maps indicate the beam and a 1" scale, respectively. For the radial profiles, the major beam of each observations is indicated by the bars in the top right corner.

112 4.5. DISCUSSION

Table 4.3: Summary of the various features which are exhibited by our targets and may be indicative of embedded planets. (a)

Source	Deep gas cavity	$\frac{T_{\rm B}}{\rm spirals/arcs}$	$v_{ m rot}$ spirals/arcs	$\begin{array}{c} \text{NIR} \\ \text{spirals} \end{array}$	NIR shadows	${\it Misalignment}^{(b)}$ ${\it inner/outer}$	Comments	Ref.
AA Tau	×	×	×	,	,	ı		
ABAur	`	5	5	>	×	✓ (A)		1
CQ Tau	>	`\	`\	>	>	✓ (A+G)		2
CS Cha	>	×	×	×	×	1		က
DM Tau	×	×	×	ı	ı	1	low res.	
DoAr 44	>	2	×	×	>	1		2
GG Tau	>	<b>\</b>	`	>	>	✓ (A)	multiple	4
$_{ m GMAur}$	>	×	×	×	×	$\mathbf{x}^{(\mathrm{A+G})}$	ı	2
$HD\ 100453$	>	>	>	>	>	✓ (A+G)	binary	2
$\mathrm{HD}100546$	>	×	2	>	×		•	2,2
HD 135344B	>	2	<u> </u>	>	>	1		. 23
$\mathrm{HD}139614$	×	3	×	×	>	1	low res.	2
$\mathrm{HD}142527$	>	<b>\</b>	`	>	>	✓ (A+G)	binary, warp	2
							cloud absorption	
$\mathrm{HD}169142$	>	>	>	×	5	1		2,6
$\mathrm{HD}34282$	2	×	×	×	×	✓ (A+G)		2
$\mathrm{HD}97048$	>	×	×	×	×	ı	cloud absorption	2
HP Cha	×	>	>	ı	1	<b>✓</b> (A)	cloud absorption	
$\operatorname{IP}\operatorname{Tau}$	×	×	×	×	×	$\mathbf{x}^{(\mathrm{A+G})}$	cloud absorption	2
IRS 48	>	×	×	ı	1	1	cloud absorption	
J1604	`	×	2	×	>	1		7
LkCa 15	2	2	<u> </u>	×	5	1		2,8
$\overline{\mathrm{MWC}}$ 758	<b>\</b>	×	×	>	×	✓ (A)		6
PDS70	>	×	×	×	×	× (A+G), (A)	imaged planets	2

Table 4.3 continued.

Source	Deep gas cavity	$T_{ m B}$ spirals/arcs	$v_{ m rot}$ spirals/arcs	NIR spirals	NIR shadows	$Misalignment^{(b)}$ $inner/outer$	Comments	Ref.
PDS99	>	×	×	1	1	ı	cloud absorption	
RXJ1615	×	×	×	×	×	$ imes (\mathrm{A+G})$		2
RXJ1852	>	×	×	×	×			10
m RYLup	×	×	×	5	×	✓ (A+G)		2,11
$\operatorname{RY}\operatorname{Tau}$	×	×	×	×	×	1		12
${ m SR}21$	×	×	×	>	×	•	cloud absorption	13
Sz91	>	5	5	×	×	•	cloud absorption	14
$\operatorname{SZ}\operatorname{Cha}$	×	5	×	×	>	$ imes (\mathrm{A+G})$	low resolution	2
							cloud absorption	
$_{ m TCha}$	×	×	×	×	×			9
$_{ m TWHya}$	×	>	>	×	×	<b>✓</b> (A)		16
$\operatorname{UX}\operatorname{Tau}\operatorname{A}$	×	>	>	>	×		binary	2
m V1247Ori	×	5	2	>	`	✓ (A+G)		2
$\rm V4046Sgr$	×	×	×	×	×	(A) >	binary	17

Notes. (a) Green checkmarks point out a detection, red crosses a non-detection, and brackets indicate if a detection is tentative. The absence of substructures does not necessarily imply the absence of a companion/planet but may be a resolution/sensitivity effect. (b) A: Obtained from ALMA continuum data in Francis & van der Marel (2020), A+G: Obtained from ALMA CO and GRAVITY data in Bohn et al. (2022)

(2022) (original reference can be found in this paper); (3) Ginski et al. (2018); (4) Keppler et al. (2020); (5) Garufi References. For spirals and shadows observed in the NIR scattered light. (1) Boccaletti et al. (2020); (2) Bohn et al. et al. (2016); (6) Pohl et al. (2017); (7) Pinilla et al. (2018); (8) Thalmann et al. (2016); (9) Benisty et al. (2015); (10) Villenave et al. (2019); (11) Langlois et al. (2018); (12) Takami et al. (2013); (13) Muro-Arena et al. (2020); (14) Tsukagoshi et al. (2014); (15) Pohl et al. (2017); (16) de Boer et al. (2020); (17) Avenhaus et al. (2018). 114 4.5. DISCUSSION

#### 4.5.1 Clear spiral or arc-like features

A few discs show clear spiral or arc-like structures in both the brightness temperature and the velocity residuals (Fig. 4.7): CQ Tau (Wölfer et al. 2021), GG Tau, HD 100453 (Rosotti et al. 2020a), HD 142527 (Garg et al. 2021), HD 169142, HP Cha, TW Hya (Teague et al. 2019b), and UX Tau A (Ménard et al. 2020). Half of these discs (CQ Tau, GG Tau, HD 100453, and HD 142527) are also marked by a spiral in the NIR, deep gas cavities, shadows in the NIR, and a misalignment between the inner and outer disc (Francis & van der Marel 2020; Bohn et al. 2022). These four systems represent the best candidates for planet-disc or companion-disc interactions. In the cases of GG Tau, HD 100453, and HD 142527, binary components are indeed known, likely causing (at least part of) the observed spiral structures. Among these eight discs, HD 142527 and HP Cha are affected by cloud absorption on the redshifted and blueshifted sides, respectively; however, this is unlikely to explain the arc features on the blueshifted side of HD 142527 or the redshifted spiral in HP Cha.

#### 4.5.2 Tentative spiral or arc-like features

Some of the discs show tentative features (spirals, arcs, or bright spots): for AB Aur, HD 135344B (see also Casassus et al. 2021), LkCa 15, Sz91, and V1247 Ori these are seen in both the brightness temperature and the velocity, with the ones in AB Aur and HD 135344B, which are also marked by most other features, being the most convincing. In addition to that, features are present in the brightness temperature residuals of DoAr 44, HD 139614, and SZ Cha and in the velocity residuals of HD 100546 and J1604. Most of these discs have deep gas cavities and are marked by shadows in the NIR; for the other cases (e.g., HD 139614 or SZ Cha), a deep cavity may be resolved with higher spatial resolution. Four of the ten sources with tentative features exhibit spirals in the NIR. It is important to note that some of the arc features may result from the misfit of the vertical structure (or other disc parameters) rather than dynamical interactions (see Fig. 12 in Yen & Gu 2020). Furthermore, some discs are strongly marked by cloud absorption. For example, the asymmetries seen in the brightness temperature of SZ Cha may result from this effect. For AB Aur, HD 100546, HD 139614, HD 135344B, and Sz 91, the residuals of the additional lines (shown in the Appendix) partly support the detection of the described features.

## 4.5.3 No spiral or arc-like features

Among the remaining sources that do not show any substructures in the kinematics or brightness temperature, most are in general marked by only a few of the indicators listed in Table 4.3 (except for a deep gas cavity). The only sources that have clearly observed NIR spirals are MWC 758 and SR 21. The lack of substructures in the brightness temperature and kinematics does not necessarily imply that there are no planet–disc interactions, but they may be unresolved instead. Besides simply being an effect of missing spatial or spectral resolution, the position and mass of an embedded planet can also result in the absence of detectable

substructures. For example, a planet closer to the star embedded in a deep cavity is more difficult to trace with the chosen methods, which are mostly able to reveal substructures on larger scales. To confirm the presence or absence of features and identify different trends, more homogeneous follow-up observations are needed.

#### 4.5.4 Conclusive remarks

Within our sample, eight discs are marked by clear substructures. In all cases, features are seen in the gas temperature and the kinematics – indicating a connection – alongside other substructures in the gas and dust. Ten other discs show tentative features, of which half present signatures in the brightness temperature and kinematics simultaneously. Half of our sample is not showing any substructures in the ALMA data besides a deep gas cavity.

Except for MWC 758 and SR 21, all targets that exhibit clear spirals in NIR scattered light show at least tentative features in the brightness temperature and/or kinematics. Scattered light is tracing the hot upper disc layers, most likely to show spirals, and since <sup>12</sup>CO is also tracing the disc surface, we expect to observe these features there as well (Law et al. 2021b). However, many of the tentative features in our sample are not spirals, which is likely related to poor spatial resolutions as well as cloud absorption in some cases. To resolve the spirals expected from the NIR, high sensitivity and spectral and spatial resolution ALMA data are crucial. For the targets showing cloud absorption, deep observations of the less affected <sup>13</sup>CO may help to resolve clear substructures. Two targets (HP Cha and TW Hya) show clear spiral structures without a counterpart having been observed yet in the NIR.

It is expected that substructures such as spirals are more likely found in systems with high luminosity and a wide cavity, where the upper disc layers can reach higher temperatures, making it much easier to observe them (e.g., Garufi et al. 2018; van der Marel et al. 2021). We searched for such correlations in our data set: while we did not find any clear trends, most discs that show no spiral substructures indeed represent the less massive, cooler, and less luminous stars, and features tend to become more visible for the more luminous sources. Given, however, the inhomogeneity of our sample, we expect a large observational bias and, to draw clear conclusions on correlations, it is crucial to study a more uniform (in terms of resolution) data set that includes a wide range of spectral types and stellar masses. As shown for TW Hya, for which very high sensitivity data exist at high spatial resolution ( $\sim 8\,\mathrm{au}$ ), substructures can still be distinguished despite a sub-solar stellar mass and an almost face-on disc. To understand if there exist differences between the different stellar groups, comparable observations are essential.

Connected to that, the lack of features cannot be seen as an indication of missing embedded planets. PDS 70, for example, hosts two confirmed massive planets, which have been directly imaged, but it does not show any other features in our data despite a deep gas cavity. This is likely because the planets are located further inside the cavity in this system and higher sensitivity plus resolution observations are needed to reveal substructures, which are related to dynamical interactions, in the temperature and the kinematics.

116 4.6. SUMMARY

Furthermore, as shown by Izquierdo et al. (2021), an embedded planet has to be rather massive to excite strong observable signatures in the kinematics: from simulations the authors find strong perturbations for planets more massive than  $1 M_{\rm J}$ ; however, to pick these up in ALMA data, very high spectral and spatial resolution is essential. Thus it is not surprising that in our sample the clearest features are seen in the multiple star systems.

## 4.6 Summary

In this work, we have analysed the brightness temperatures and kinematics of a sample of 36 large cavity transition discs, representing the best candidates to search for dynamical interactions. Our main results are summarized as follows.

- Eight discs out of our sample show significant perturbations in both the brightness temperature and velocity residuals, while no features are seen in half of the sample at the current (spatial and spectral) resolution and sensitivity.
- Several discs show tentative features that need to be confirmed with deep, high resolution ALMA observations in the upcoming years.
- Almost all targets that exhibit spirals in NIR scattered light show at least tentative features in the CO data.
- In most cases our method reveals deviations that are caused by sub-stellar companions.
- For about 60% of the sources, a deep gas cavity is resolved in addition to the dust cavity at the current spatial resolution.

To detect planets in the Jupiter-mass range, the available observations are neither deep enough nor do they have the required spatial and spectral resolution, explaining the lack of features in many discs. Upcoming and future deep ALMA observations at high spectral and spatial resolution together with dedicated modelling efforts may reveal more of such features and help to disentangle different formation scenarios.

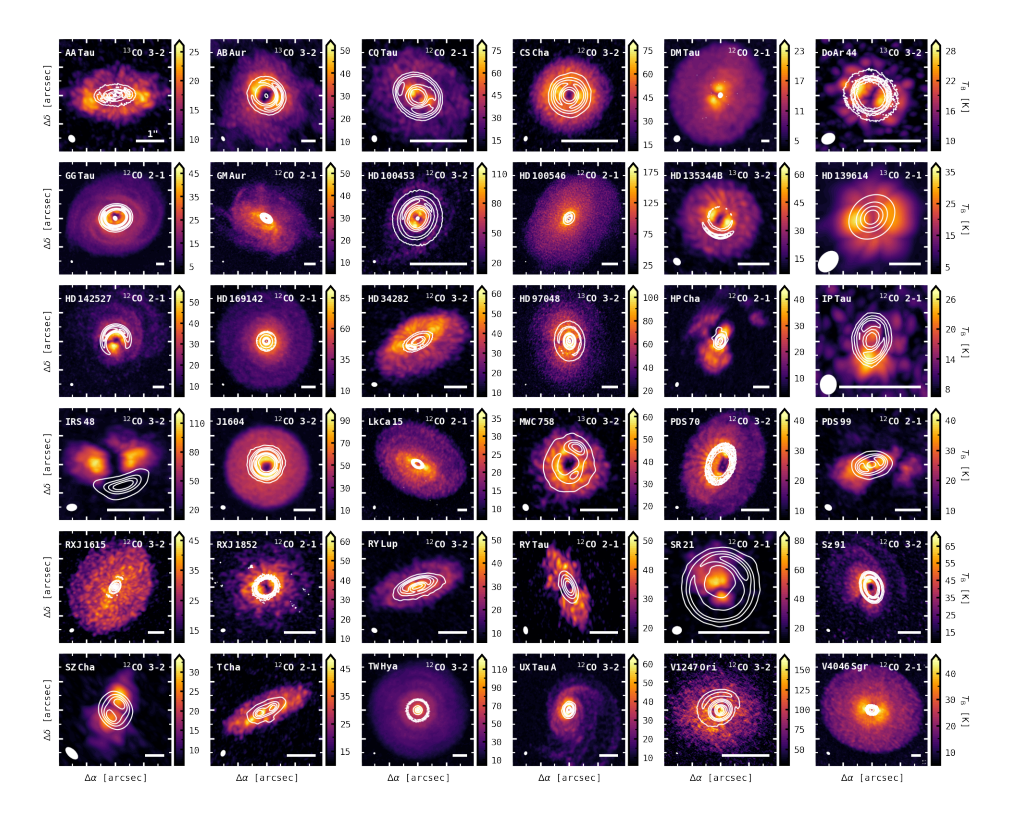
## Acknowledgements

We greatly thank the referee Ruobing Dong for his helpful feedback that improved the quality of this work. We also would like thank all the people that kindly provided the re-imaged/self-calibrated data sets. This paper makes use of different ALMA data sets, detailed in Tables 4.2 and 4.E.1. ALMA is a partnership of ESO (representing its member states), NSF (USA) and NINS (Japan), together with NRC (Canada) and NSC and ASIAA (Taiwan) and KASI (Republic of Korea), in cooperation with the Republic of Chile. The Joint ALMA Observatory is operated by ESO, auI/NRAO and NAOJ.

## Appendix

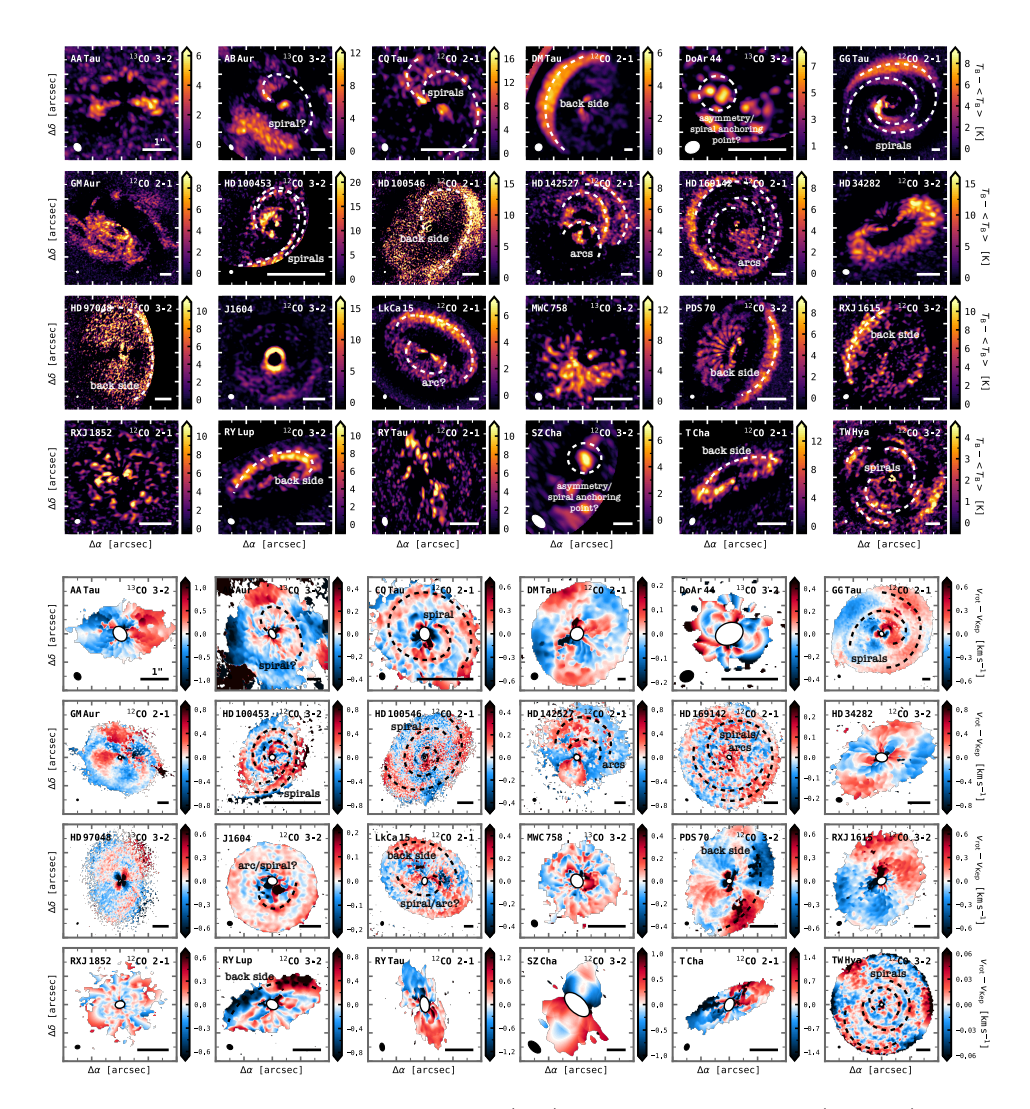
### 4.A Continuum

Figure 4.A.1 shows the peak brightness temperature maps of the main lines used for the analysis in this work with overlaid millimetre continuum (either ALMA B6 or B7). For most cases, the size of the dust disc is substantially smaller than that of the gas disc.



**Figure 4.A.1:** Peak brightness temperature maps of the gas emission in our targets, shown for the main CO lines with the continuum overlaid as white contours. Five contour levels are equally spaced between  $3\sigma$  and the peak flux of the continuum. The circle and bar in the bottom left and bottom right corner of each panel indicate the beam and a 1" scale, respectively.

## 4.B Thick disc residuals of the main lines



**Figure 4.B.1:** Brightness temperature (top) and rotation velocity (bottom) residuals, shown for the main lines used in this analysis and for a thick disc geometry. The circle and bar in the bottom left and bottom right corner of each panel indicate the beam and a 1" scale, respectively. Some features are annotated.

## 4.C Uncertainties of the rotation velocity

In Fig. 4.C.1, we show the uncertainties of the kinematics for the main lines, computed with Bettermoments. These statistical uncertainties were calculated by linearising and propagating the uncertainty from the fluxes to the centroid estimate. The uncertainties mostly lie well below the channel width, but increase in the central regions due to beam smearing. For lower sensitivity observations, thermal broadening plays an important role, significantly increasing the uncertainties.

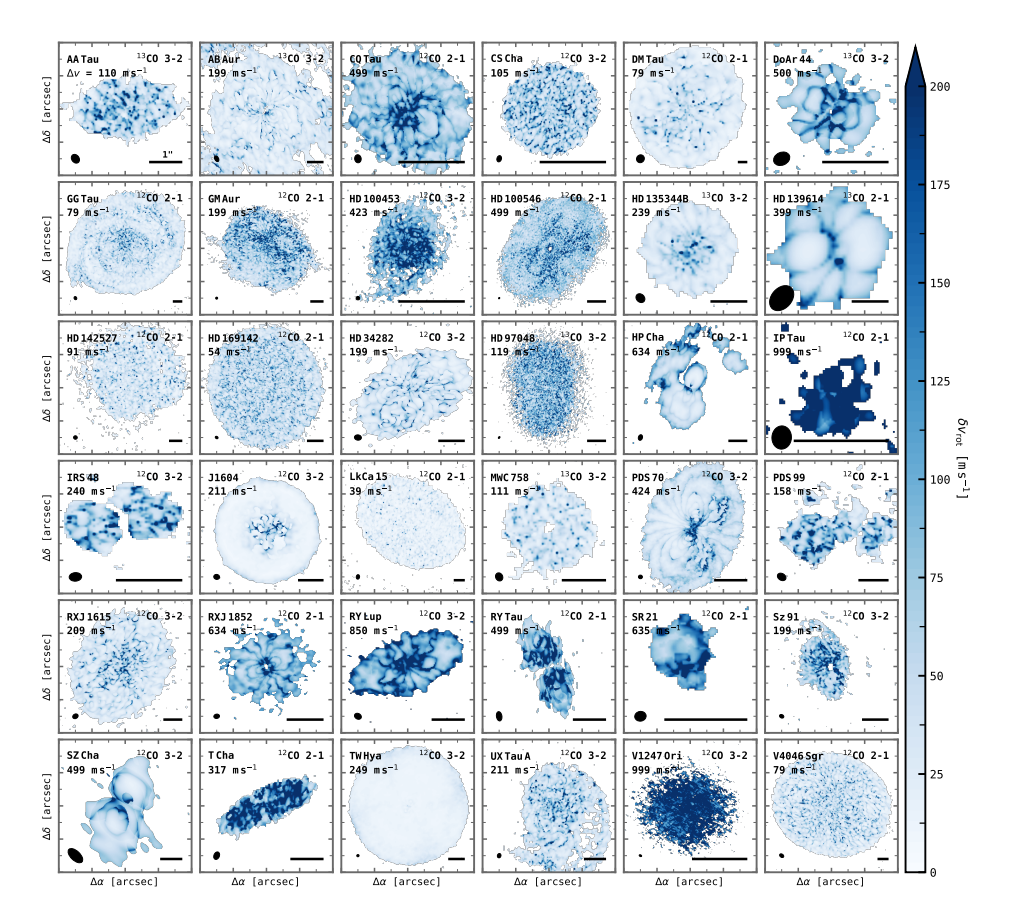


**Figure 4.C.1:** Kinematical uncertainties of the main lines of this analysis, computed with BETTERMOMENTS. The circle and bar in the bottom left and bottom right corner of each panel indicate the beam and a 1" scale, respectively. The channel spacing is shown in the top left corner of each panel.

# 4.D Re-imaged and archival data products comparison

In this work, we have combined re-imaged with archival data products and it is important to understand what impact this has on the results. When re-imaged sets were available, we conducted our analysis for both the re-imaged and the according archival image cubes and compared the results. A few examples are shown in Fig. 4.D.1 for a disc with clear spirals, two discs with tentative spirals, and one without any observed features. We find that the fitting procedure is not significantly affected by the choice of cube: the detection of clear spirals as well as a non-detection do not depend on the data set. Due to an increased S/N, tentative features come out stronger (e.g., J1604) and in some cases only become visible (e.g., HD 135344B) in the re-imaged products, thus some tentative substructures may be hidden in the cases that we classify as non-detections, when the archival product data were used.

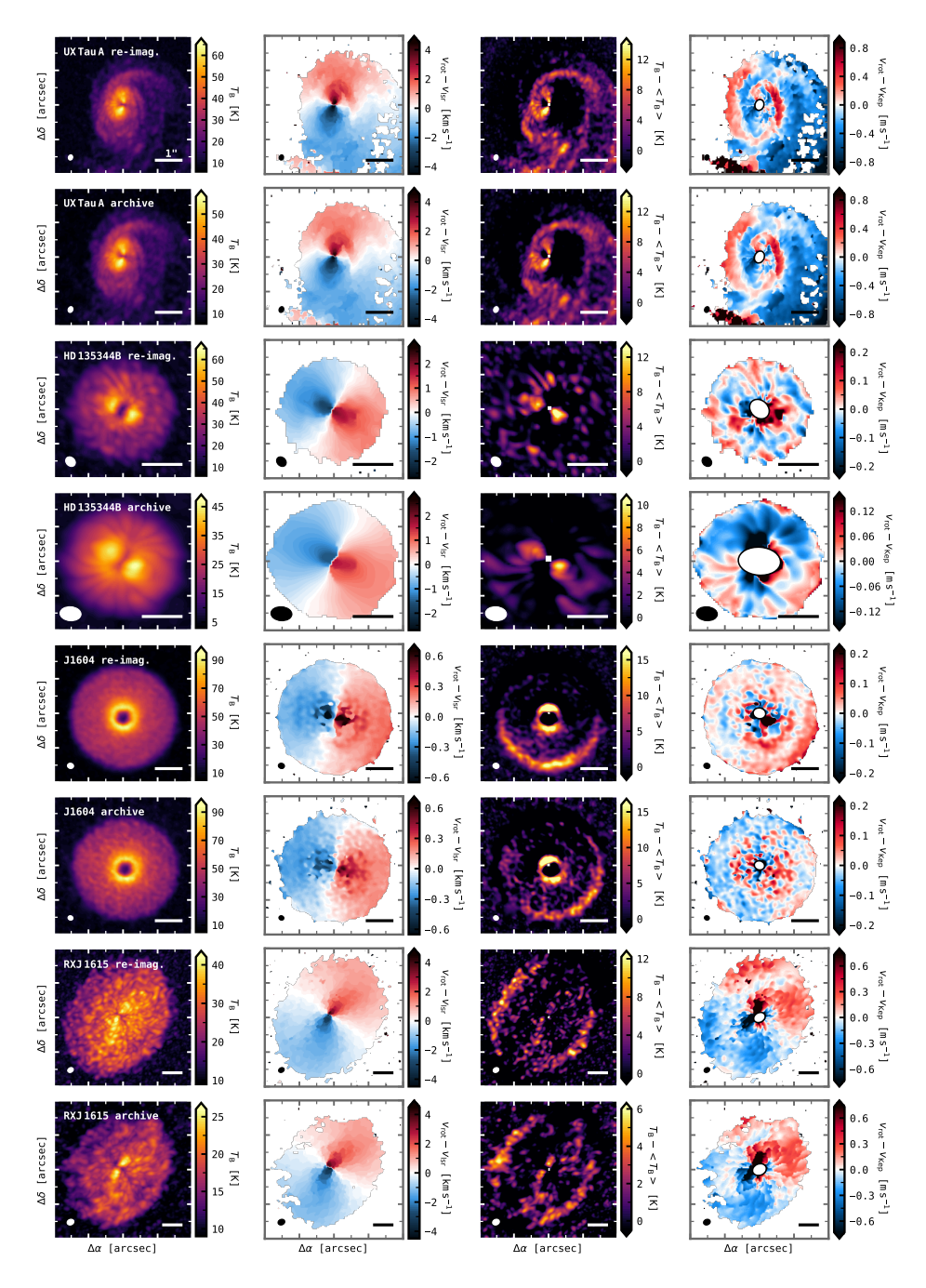


**Figure 4.D.1:** Comparison between the re-imaged and archival data for four sample sources, including one with clear spirals, two with tentative features, and one without any features. The circle and bar in the bottom left and bottom right corner of each panel indicate the beam and a 1" scale, respectively.

#### 4.E Additional lines

This appendix comprises the results for the additional lines used in this work. When studying substructures in discs, it is useful to look at various molecular tracers that probe different disc layers. Understanding if and how substructures vary vertically and radially can be used to assess the underlying perturbation. For example, in a passively heated disc with a vertical temperature gradient, the opening angle of a spiral is expected to decrease towards the midplane; whereas, for spirals launched by gravitational instability the midplane would be heated by shocks, resulting in similarly wound spirals throughout the disc (Juhász & Rosotti 2018).

#### 4.E.1 Characteristics

Some characteristics of the data are listed below in Table 4.E.1. In most cases, the archival data products were used for the analysis, as indicated in the last column.

Table 4.E.1: Characteristics of the additional ALMA line data.

Object	Line	Project ID	Beam (")	$\Delta v \; (\mathrm{km}  \mathrm{s}^{-1})$	$RMS (mJy beam^{-1})$	$source^{(a)}$
ABAur	$^{12}CO \ 3-2$	2012.1.00303.S	$0.31 \times 0.19$	0.05	11.4	P/PC
	$^{12}{ m CO}~2-1$	2015.1.00889.S	$0.11\mathrm{x}0.08$	0.32	3.5	A
	$^{13}$ CO, $^{18}$ O 2-1	2019.1.00579.S	0.95x0.57	0.17	9.5, 7.9	A
CQTau	$^{13}$ CO 2-1	2013.1.00498.S	0.13 x 0.1	0.7	6.0	$\mathrm{P/PC}$
		2016.A.00026.S				
		2017.1.01404.S				
$_{ m DMTau}$	$^{12}CO\ 3-2$	2013.1.00647.S	$1.0 \times 0.75$	0.2	55.9	A
	$^{13}$ CO, $^{18}$ O 3-2	2016.1.00565.S	$0.37 \times 0.29, 1.04 \times 0.81$	0.11	16.8, 21.4	A
	$^{13}$ CO, $^{18}$ O 2-1	2016.1.00724.S	0.9x0.84	80.0	19.2, 14.1	A
GGTau	$^{12}$ CO, $^{13}$ CO 3-2	2012.1.00129.S	0.4x0.3	0.25	5.7, 7.8	A
$_{ m GMAur}$	$^{13}$ CO 3-2	2016.1.00565.S	$0.38 \times 0.26$	0.11	16.2	A
	$^{13}$ CO, $^{18}$ O 2-1	2018.1.01055.L	$0.15 \times 0.15, 0.17 \times 0.13$	0.2	2.7, 1.1	$\mathrm{P/PC}$
$\mathrm{HD}100546$	$^{12}CO\ 3-2$	2011.0.00863.S	0.94x0.42	0.11	19.4	A
	$^{13}$ CO, $^{18}$ O 2-1	2016.1.00344.S	$0.25\mathrm{x}0.14$	0.17	6.8, 6.4	A
HD135344B	$^{12}CO\ 3-2$	2012.1.00870.S	0.36 x 0.29	0.11	38.9	A
	$^{12}$ CO, $^{13}$ CO, $^{18}$ O 2-1	2018.1.01066.S	$0.1\mathrm{x}0.08$	0.2	2.6, 2.8, 2.4	$\mathrm{P/PC}$
HD139614	$C^{18}O$ 2-1	2015.1.01600.S	0.73x0.53	0.33	11.9	A
HD142527	$^{12}CO\ 3-2$	2011.0.00465.S	0.57 x 0.35	0.5	11.1	$\mathrm{P/PC}$
	$^{13}$ CO, $^{18}$ O 3-2	2012.1.00725.S	$0.31 \mathrm{x} 0.27$	0.11	8.0, 9.9	A
	$^{13}$ CO, $^{18}$ O 2-1	2015.1.01353.S	0.29x0.26, 0.84x0.77	0.1	7.5, 19.3	A
HD169142	$^{12}$ CO, $^{13}$ CO 3-2	2012.1.00799.S	0.18x0.13, 0.19x0.13	0.21, 0.22	17.9, 19.8	A
	$^{13}$ CO, $^{18}$ O 2-1	2015.1.00490.S	0.19x0.14	0.08	5.4, 4.0	Α
HD34282	$^{12}$ CO, $^{13}$ CO, $^{18}$ CO 2-1	2015.1.00192.S	0.24x0.21, 0.25x0.23	0.08, 0.17	10.6, 7.9, 5.5	A
HD97048	$^{12}CO\ 3-2$	2013.1.00658.S	$0.65 \times 0.39$	0.2	13.93	A
	$^{12}$ CO, $^{13}$ CO, $^{18}$ O 2-1	2015.1.00192.S	0.46x0.22	0.3	6.9, 6.5, 6.30, 4.9	$\mathrm{P/PC}$
HPCha	$^{12}CO\ 3-2$	2013.1.01075.S	0.77x0.4	0.2	35.7	A
IRS48	$^{13}$ CO 3-2	2013.1.00100.S	$0.21 \times 0.16$	0.26	14.4	Α

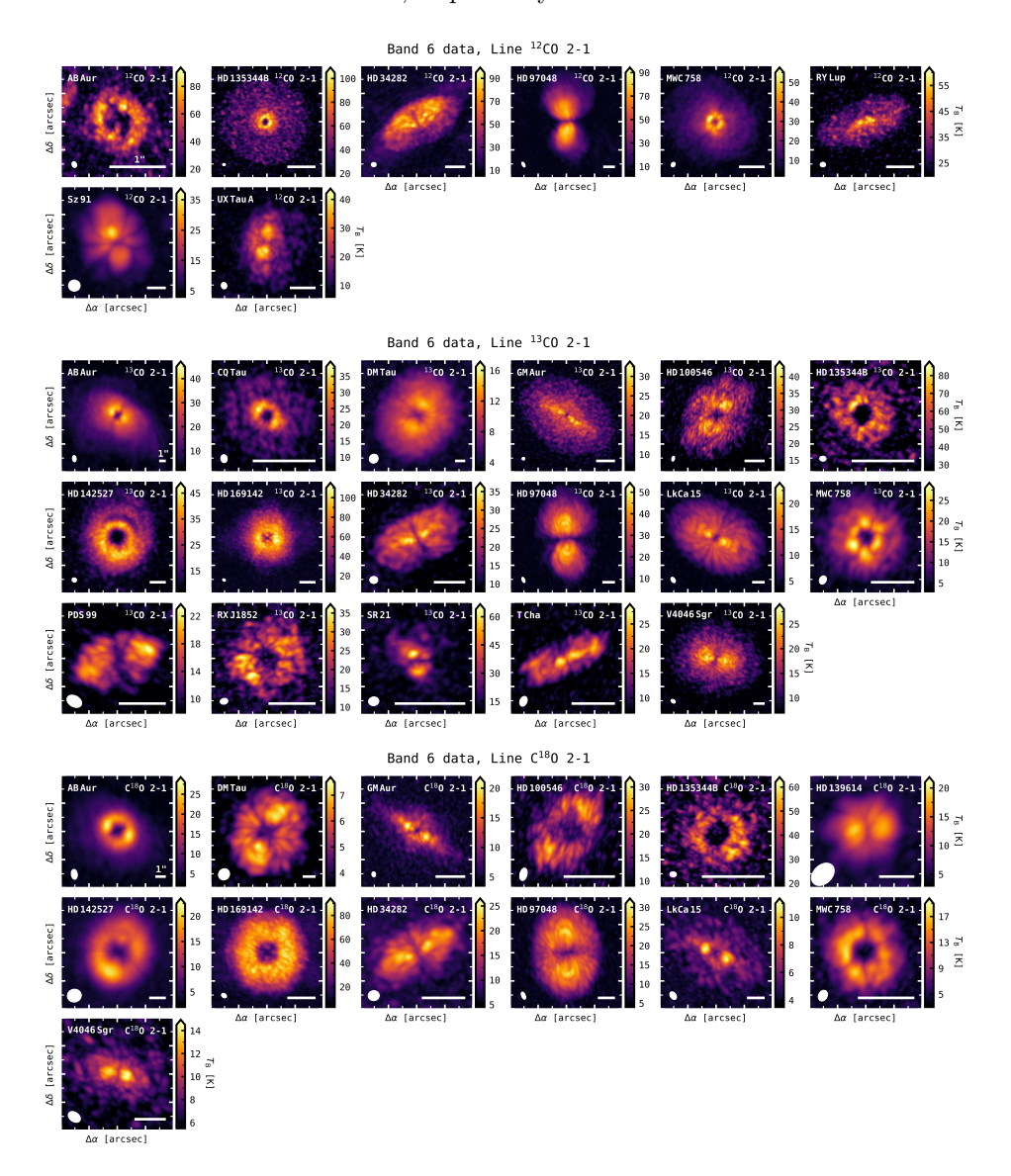
Table 4.E.1 continued.

Object Line	Line	Project ID	Beam (")	$\Delta v \; (\mathrm{km}\mathrm{s}^{-1})$	$RMS (mJy beam^{-1})$	$Source^{(a)}$
LkCa15	$^{13}$ CO, $^{18}$ O 2-1	2018.1.00945.S	0.48x0.3	0.33	3.7, 4.8	P/PC
MWC758	$^{12}CO\ 3-2$	2011.0.00320.S	0.82x0.47	0.05	37.3	A
	$C^{18}O$ 3-2	2012.1.00725.S	0.34x0.22	9.0	26.1	A
	$^{12}$ CO, $^{13}$ CO, $^{18}$ O 2-1	2017.1.00940.S	0.2x0.15	1.26, 1.33	1.7, 1.6, 1.2	A
PDS99	$^{13}$ CO 2-1	2015.1.01301.S	0.34x0.23	0.17	8.6	A
RXJ1852	$^{13}$ CO 2-1	2018.1.00689.S	$0.16 \mathrm{x} 0.12$	99.0	4.8	A
$\mathrm{RYLup}$	$^{12}CO \ 2-1$	2017.1.00449.S	0.19x0.16	0.04	15.7	A
SR21	$^{13}$ CO 3-2	2012.1.00158.S	0.27x0.23	0.24	11.5	A
	$^{13}$ CO 2-1	2018.1.00689.S	$0.15 \mathrm{x} 0.12$	99.0	5.1	A
$_{ m Sz91}$	$^{12}CO \ 2-1$	2013.1.00663.S	$0.62 \times 0.59$	0.5	27.6	A
TCha	$^{12}CO,  ^{13}CO  3-2$	2012.1.00182.S	$0.26 \times 0.14, 0.27 \times 0.14$	0.85, 0.88	14.5, 17.4	A
	$^{13}$ CO 2-1	2017.1.01419.S	0.24x0.16	1.33	5.0	A
VXTauA	$^{12}CO \ 2-1$	2013.1.00498.S	$0.26 \times 0.21$	0.63	7.4	A
m V4046Sgr	$^{12}$ CO, $^{13}$ CO 3-2	2016.1.00315.S	0.28x0.17, 0.3x0.18	0.21, 0.44	25.4, 22.5	A
	$^{13}$ CO, $^{C18}$ CO 2-1	2016.1.00724.S	0.42x0.3	80.0	11.4, 7.8	A

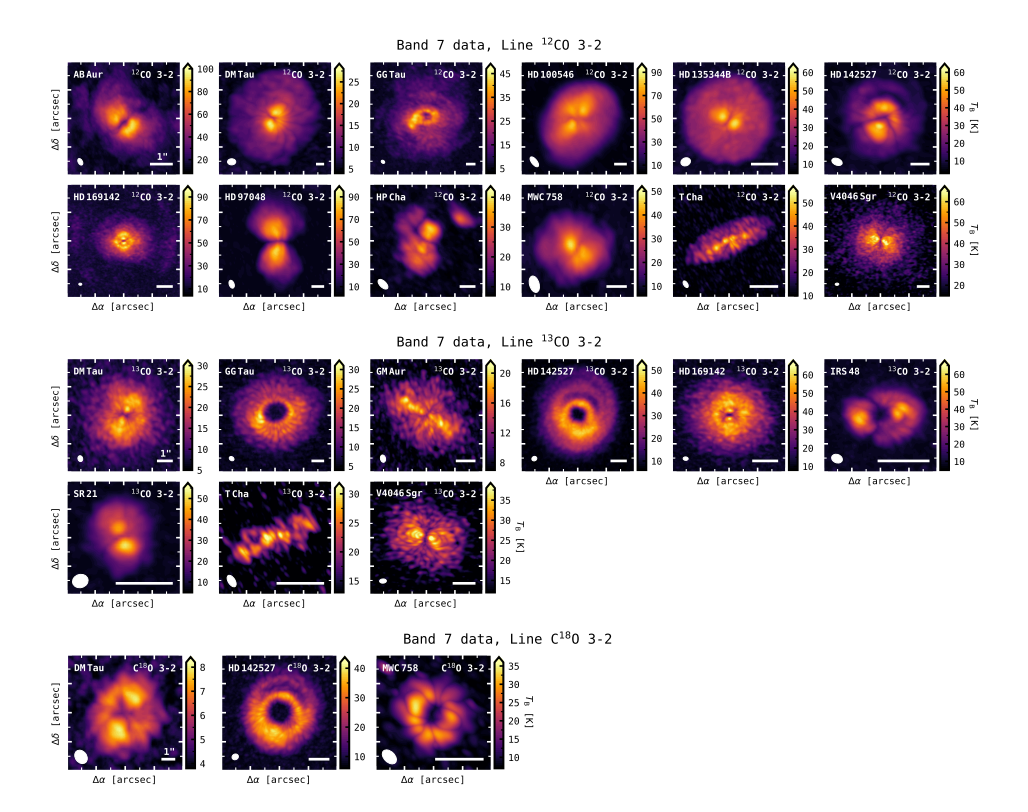
References. AB Aur: van der Marel et al. (2021); CQ Tau: Wölfer et al. (2021); GM Aur: Öberg et al. (2021); Huang et al. (2021); HD 135344B: Casassus et al. (2021); HD 142527: van der Marel et al. (2021); HD 97048: Stapper et al. in prep.; LkCa 15: Leemker Notes.  $^{(a)}$  P/PC: re-imaged data cube. Public data or obtained via private communication, A: archival data product. et al. (2022).

#### 4.E.2 Brightness temperature maps

Figures 4.E.1 and 4.E.2 show the brightness temperature maps for the additional CO lines in Band 6 and Band 7, respectively.



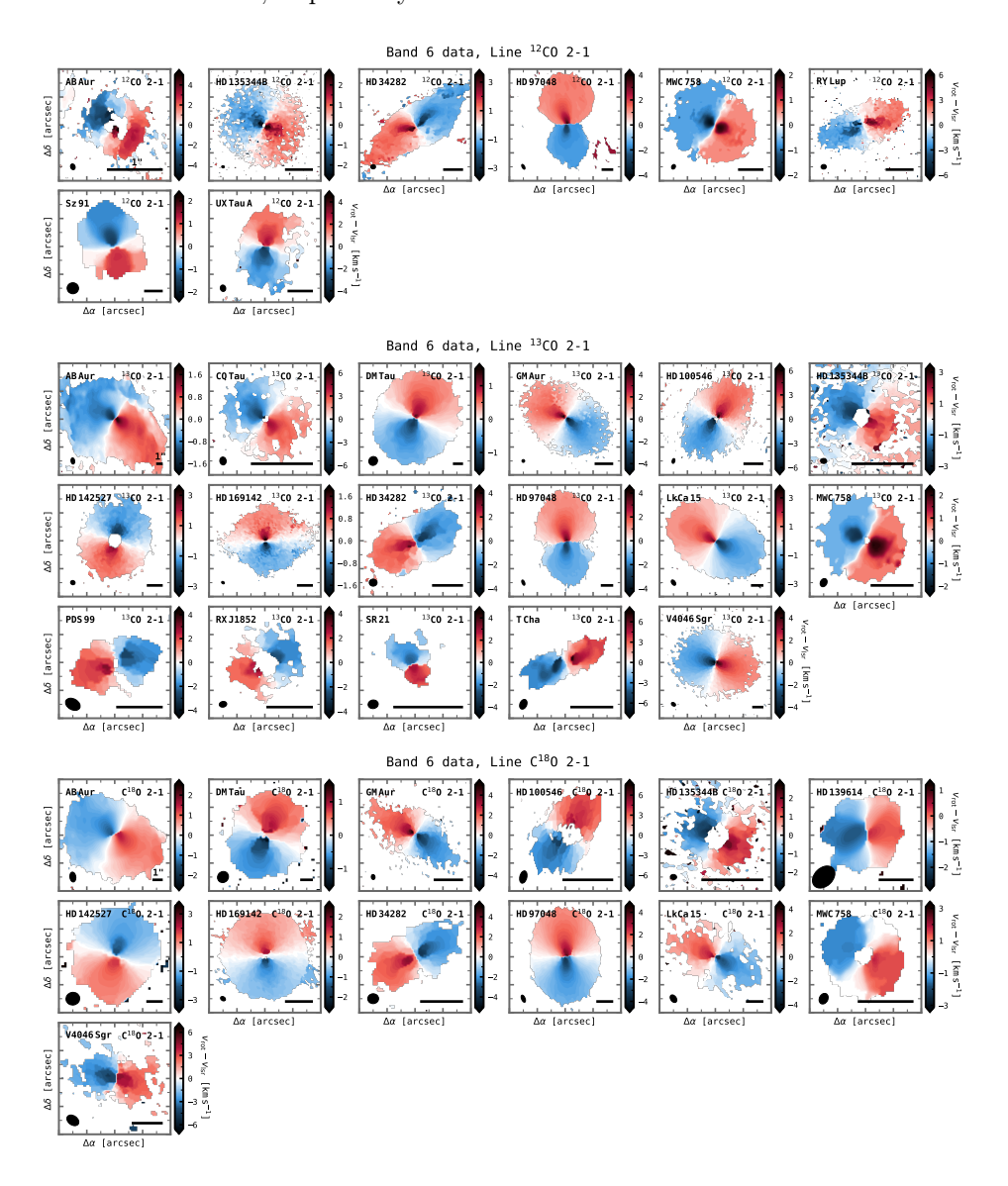
**Figure 4.E.1:** Peak brightness temperature maps of the gas emission in our targets, shown for the additional Band 6 CO lines used in this analysis. The conversion from peak intensity to units of Kelvin was done with the Planck law. The circle and bar in the bottom left and bottom right corner of each panel indicate the beam and a 1" scale, respectively.



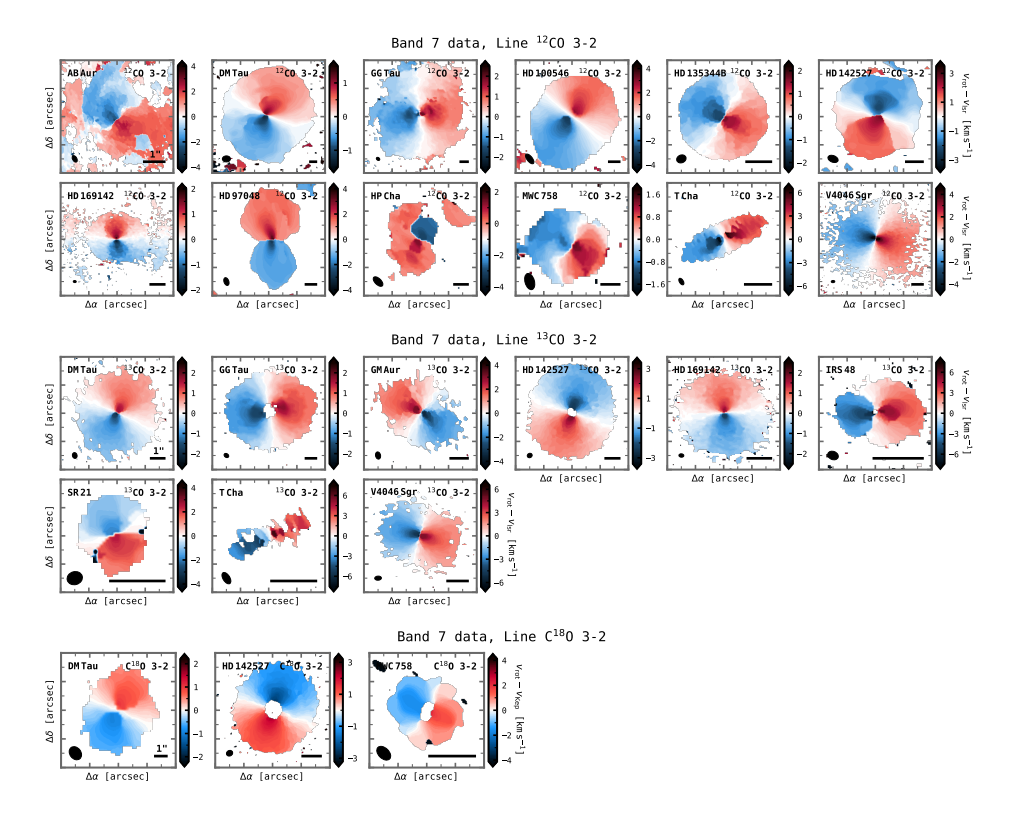
**Figure 4.E.2:** Peak brightness temperature maps of the gas emission in our targets, shown for the additional Band 7 CO lines used in this analysis. The conversion from peak intensity to units of Kelvin was done with the Planck law. The circle and bar in the bottom left and bottom right corner of each panel indicate the beam and a 1" scale, respectively.

#### 4.E.3 Rotation velocity maps

Figures 4.E.3 and 4.E.4 show the kinematical maps for the additional CO lines in Band 6 and Band 7, respectively.



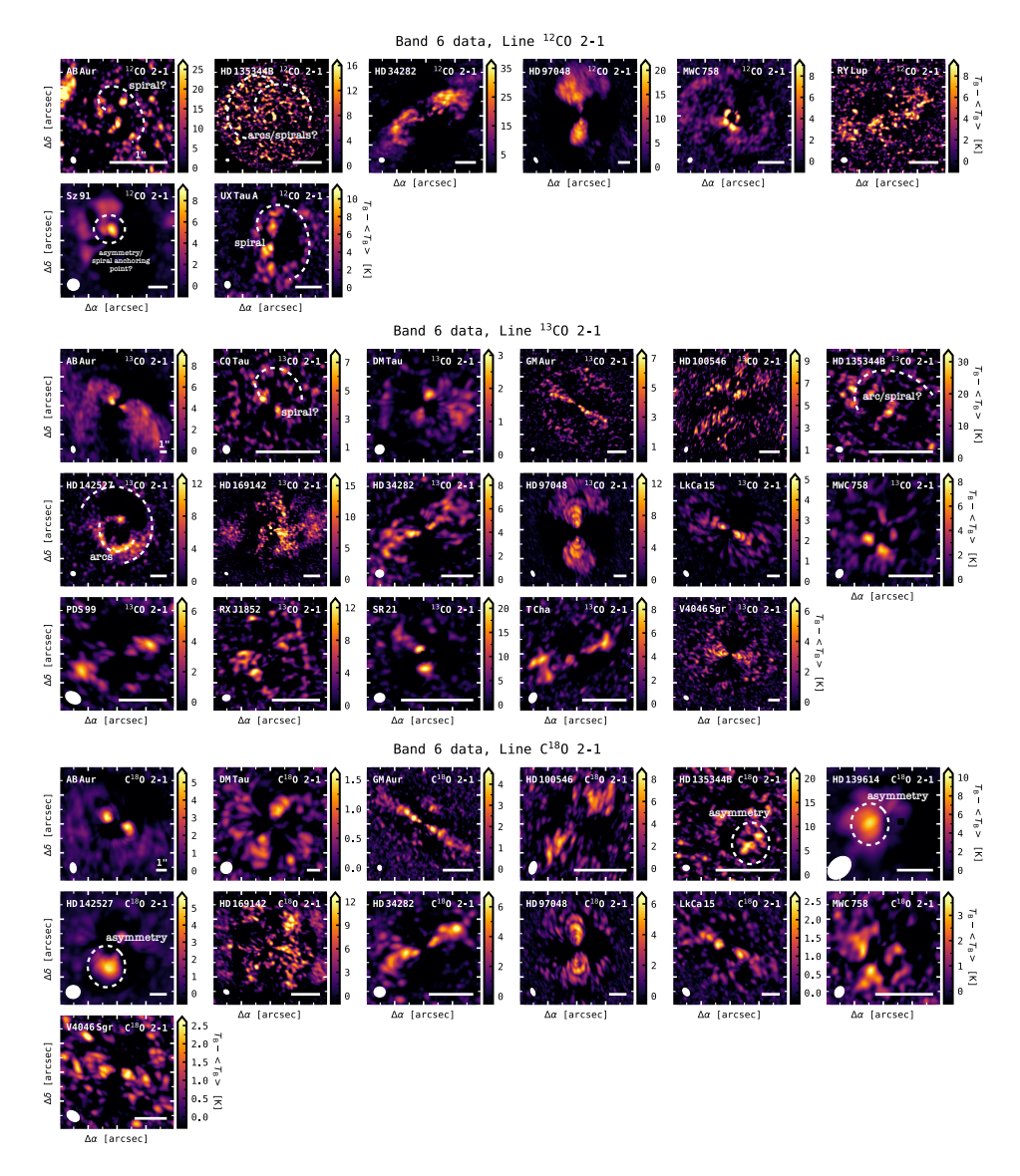
**Figure 4.E.3:** Rotation velocity maps of the gas emission in our targets, shown for the additional Band 6 lines used in this analysis. The maps were computed with BETTERMOMENTS. The circle and bar in the bottom left and bottom right corner of each panel indicate the beam and a 1" scale, respectively.



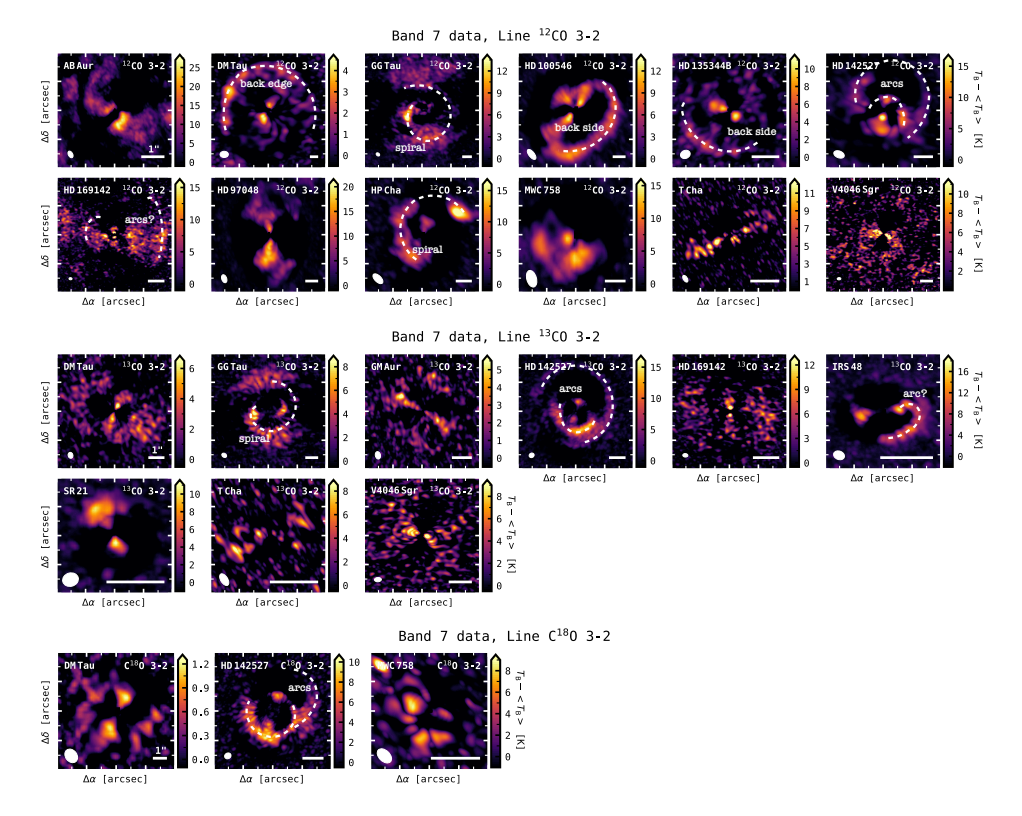
**Figure 4.E.4:** Rotation velocity maps of the gas emission in our targets, shown for the additional Band 7 lines used in this analysis. The maps were computed with BETTERMOMENTS. The circle and bar in the bottom left and bottom right corner of each panel indicate the beam and a 1" scale, respectively.

#### 4.E.4 Brightness temperature residuals

Figures 4.E.5, 4.E.6, and 4.E.7 show the brightness temperature residuals for the additional CO lines in Band 6 and Band 7 for both the thin and the thick disc geometry.



**Figure 4.E.5:** Brightness temperature residuals obtained with GOFISH, shown for the additional Band 6 lines used in this analysis and for a thin disc geometry. The circle and bar in the bottom left and bottom right corner of each panel indicate the beam and a 1" scale, respectively. Some features are annotated.



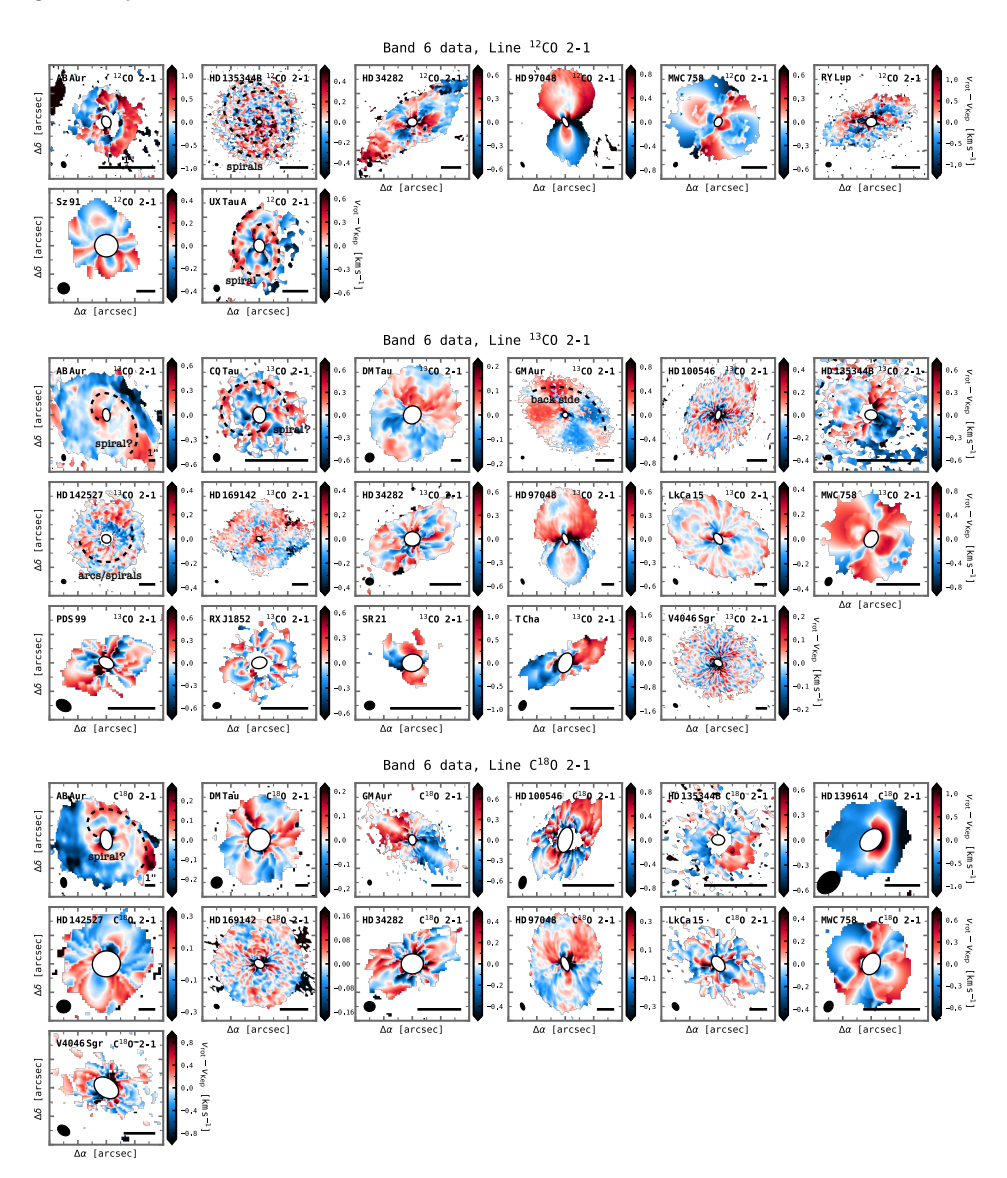
**Figure 4.E.6:** Brightness temperature residuals obtained with GOFISH, shown for the additional Band 7 lines used in this analysis and for a thin disc geometry. The circle and bar in the bottom left and bottom right corner of each panel indicate the beam and a 1'' scale, respectively. Some features are annotated.



Figure 4.E.7: Brightness temperature residuals obtained with GOFISH, shown for the additional Band 6 and Band 7 lines used in this analysis and for a thick disc geometry. The circle and bar in the bottom left and bottom right corner of each panel indicate the beam and a 1" scale, respectively. Some features are annotated.

#### 4.E.5 Rotation velocity residuals

Figures 4.E.8, 4.E.9, and 4.E.10 show the rotation velocity residuals for the additional CO lines in Band 6 and Band 7 for both the thin and the thick disc geometry.



**Figure 4.E.8:** Rotation velocity residuals obtained with EDDY, shown for the additional Band 6 lines used in this analysis and for a thin disc geometry. The circle and bar in the bottom left and bottom right corner of each panel indicate the beam and a 1" scale, respectively. Some features are annotated.

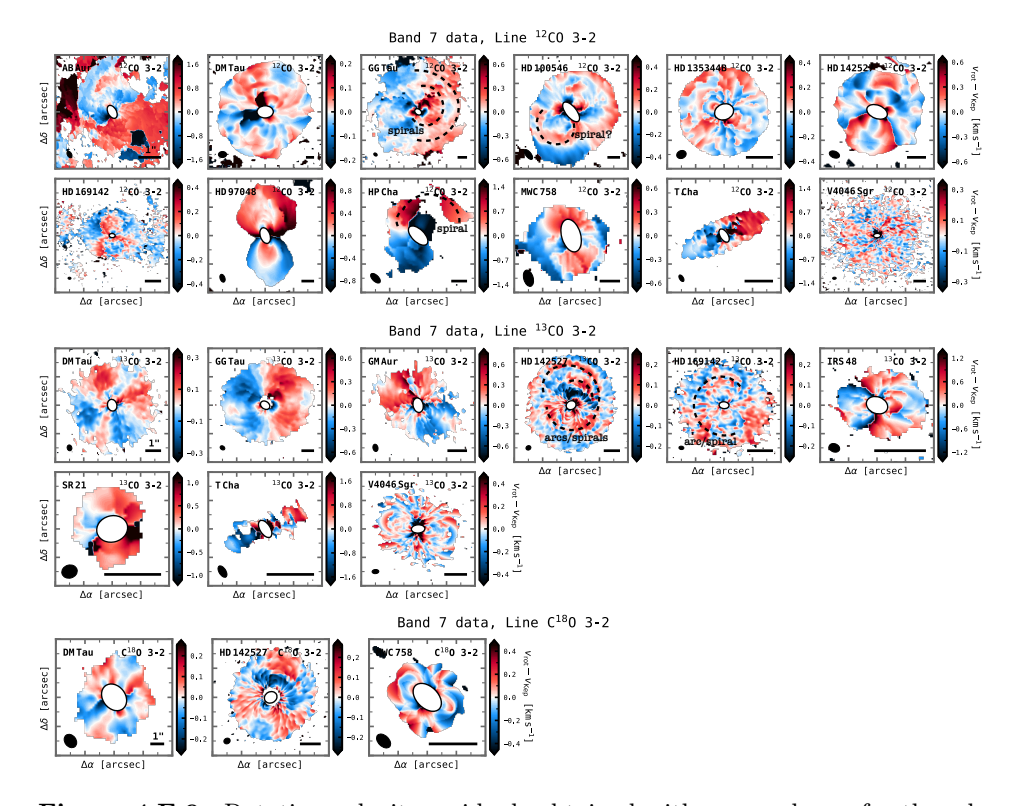


**Figure 4.E.9:** Rotation velocity residuals obtained with EDDY, shown for the additional Band 7 lines used in this analysis and for a thin disc geometry. The circle and bar in the bottom left and bottom right corner of each panel indicate the beam and a 1" scale, respectively. Some features are annotated.

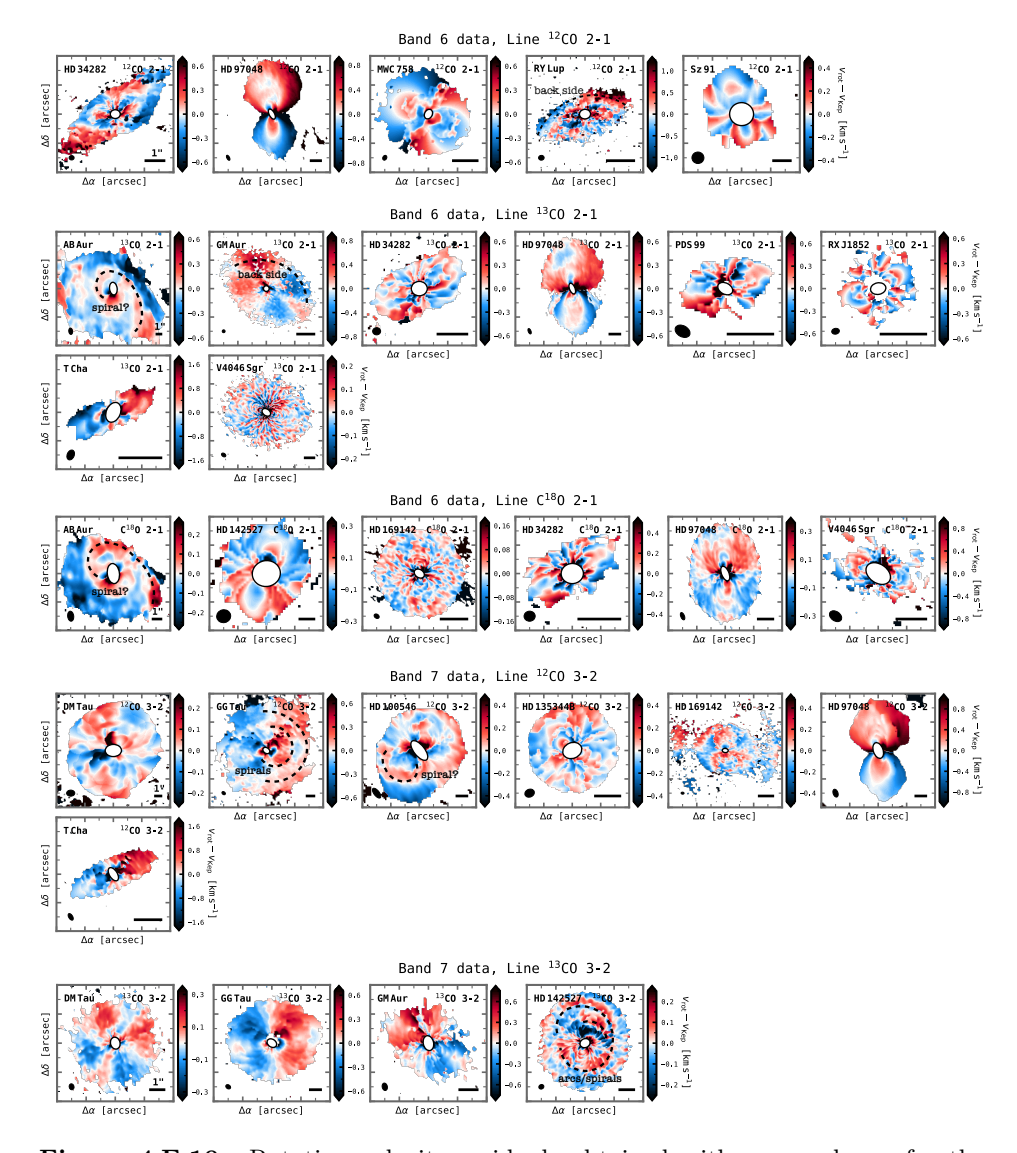


**Figure 4.E.10:** Rotation velocity residuals obtained with EDDY, shown for the additional Band 6 and Band 7 lines lines used in this analysis and for a thick disc geometry. The circle and bar in the bottom left and bottom right corner of each panel indicate the beam and a 1" scale, respectively. Some features are annotated.

## 4.F Radial profiles of the integrated intensity

Figure 4.F.1 shows the radial profiles of the integrated CO intensity. Such profiles can be used to estimate the size of the cavity. As a deep cavity, we define those cases where a clear drop in emission can been seen in the inner regions for at least the more optically thin lines that tend to trace the column density.

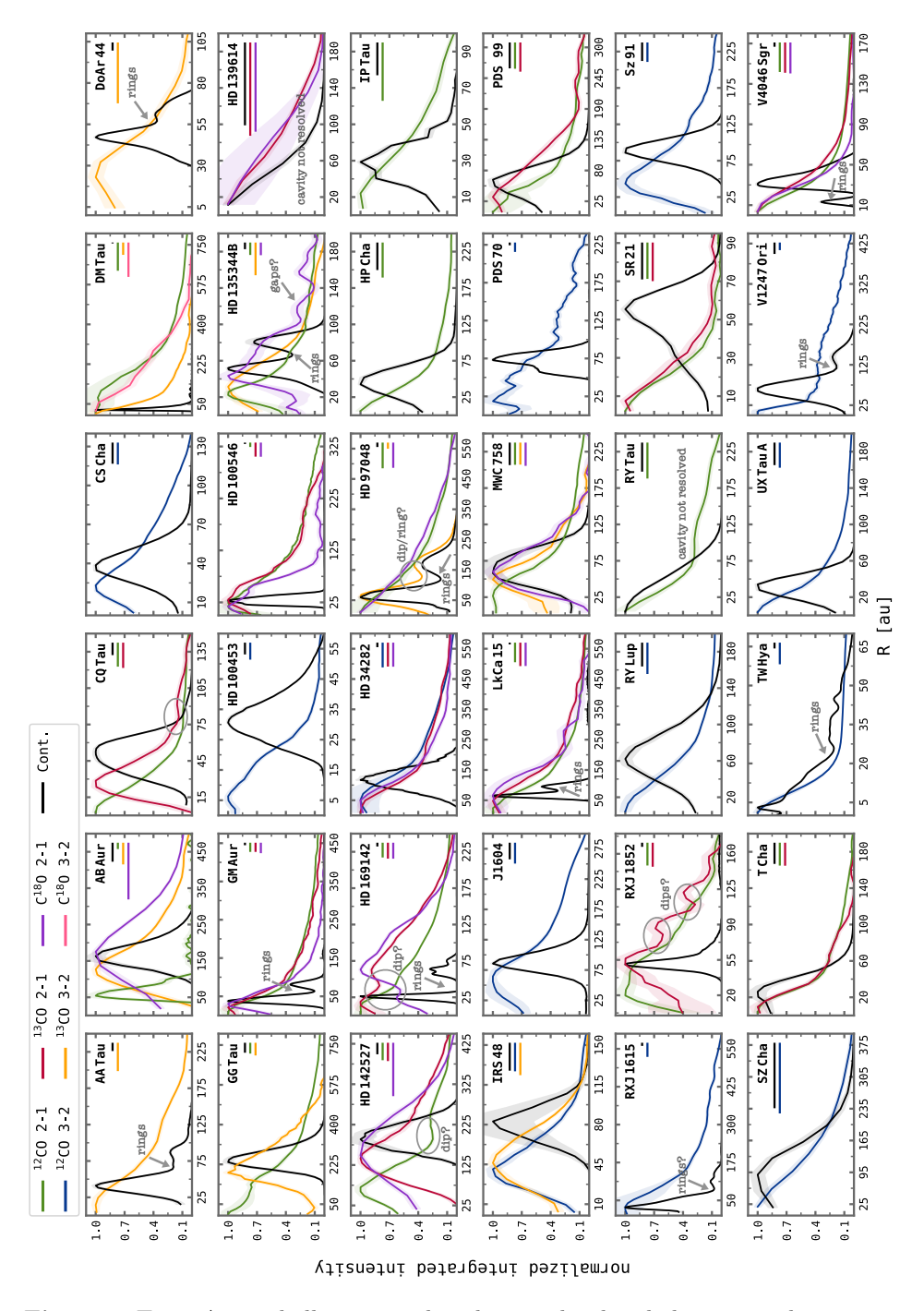


**Figure 4.F.1:** Azimuthally averaged and normalized radial integrated intensity profiles for the different CO lines (coloured lines) and continuum emission (black lines). The major beam of each observation is indicated by the bars in the top right corner. Some features of the profiles are annotated in the individual panels.